Bull. Min. Res. Exp. (2023) 171: 1-32

Bulletin of the Mineral Research and Exploration

http://bulletin.mta.gov.tr

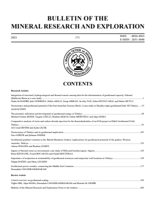

Integration of structural, hydrogeological and thermal remote sensing data for the determination of geothermal capacity: Edremit (Balıkesir) Basin as a case study

Önder KAYADİBİ[a], Şule GÜRBOĞA[a], Hafize AKILLI[a], Serap ARIKAN[a], Sevilay TAN[a], Zehra DEVECİ ARAL[a] and Halim MUTLU[b]

[a] *General Directorate of Mineral Research and Exploration, Ankara, Türkiye*
[b] *Ankara University, Department of Geological Engineering, Ankara, Türkiye*

Research Article

Keywords:
Geothermal, Remote Sensing and GIS, Tectonic, Hydrogeology, Edremit (Balıkesir) Basin.

Received Date: 23.05.2022
Accepted Date: 02.05.2023

ABSTRACT

Basins formed on active strike-slip faults are important prospect areas for geothermal energy exploration since the crust gets thinner in these areas and tectonic structures provide favorable conditions for heat-fluid circulation and transportation. The objective of the recent study is to evaluate the geothermal capacity of the Edremit Basin utilizing tectonic, geological, and hydrogeological studies, combining remote sensing (land surface temperature-LST, hydrothermal alteration, and multi-temporal InSAR (MT-InSAR) assessments). We present structural literature data and the results of field mapping, which revealed the geometry, kinematics, and dynamics of structural features, geological units as geothermal system components, thermal and cold water chemistry, and thermal infrared remote sensing analysis. For the purpose of assessing new targets and recent geothermal capacity, these data are combined and evaluated. According to the outcomes of the study, the fault pattern in the Edremit Basin is generated by N-S extension, which produced E-W dominant striking normal faults with a heritage of paleostructures oriented in various directions. According to remote sensing analyses, the primary LST regions in the basin are defined by the active faults. Therefore, a high sodium sulfate ratio recorded in the chemical analyses of the water samples indicates a deep circulation and high possibility for the presence of thermal water. Consequently, our findings are consistent with the work to include thorough field geology surveys, structural patterns, LST, and water chemistry to refined exploration process. All these results indicated that Edremit (Balıkesir) Basin holds a great promise for the discovery of new geothermal energy sources.

1. Introduction

As a result of technological developments, increasing population, industrialization, and rapid urbanization, energy requirements rise, requiring greater exploration of alternative energy resources such as wind, solar, wave, geothermal, and biomass. Geothermal energy is regarded as one of the most prominent renewable and clean energy resources in this context. Furthermore, geothermal energy has a wide range of applications despite its low environmental impact (CO_2 emissions are the lowest). The energy (heat) is transferred naturally between a heat source and a heat sink in a constrained area of the Earth's crust using a geothermal system. Accordingly, there are various specialties relating to geothermal energy, including geological engineering and geotechnologies (Zannina et al., 2020).

Citation Info: Kayadibi, Ö., Gürboğa, Ş., Akıllı, H., Arıkan, S., Tan, S., Deveci Aral, Z., Mutlu, H. 2023. Integration of structural, hydrogeological and thermal remote sensing data for the determination of geothermal capacity: Edremit (Balıkesir) Basin as a case study. Bulletin of the Mineral Research and Exploration 171, 1-32. https://doi.org/10.19111/bulletinofmre.1291349

**Corresponding author: Önder KAYADİBİ; onder.kayadibi@mta.gov.tr*

During the last two decades, a number of studies has utilized the satellite imagery (Gutiérrez et al., 2012; Hulley et al., 2012; Vaughan et al., 2012*a* and *b*; Littlefield and Calvin, 2014; Song and Park, 2014; Van der Meer et al., 2014; Hewson et al., 2017; Parastatidis et al., 2017; Sheng et al., 2009; Ramírez-González et al., 2019) to determine the fault-controlled geothermal anomalies which enable better estimation of underground temperatures (Pieri and Adams, 2004 and 2005; Faulds et al., 2006; Srivastava et al., 2009; Giordano et al., 2013; Nukman and Moeck, 2013; Norini et al., 2015; Calderón-Chaparro and Vargas-Cuervo, 2019) and volcanic systems (Braddock et al., 2017; Waswa, 2017). For this reason, attention is currently being given to the deeper zones that lie under the geothermal reservoirs in order to better understand the comparatively near-surface regions. Accordingly, near-surface and surface data, such as surface temperature values (Land Surface Temperature-LST), geothermal heat flux (GHF) values, hydrothermal alteration zones, and alteration minerals linked to geothermal resources define fault directions and types, as well as geophysical and drilling outputs, and have a direct impact on the geothermal capacity. Surface data are collected prior to the application of high-cost field applications such as geophysical and drilling studies, which significantly contribute to the exploration of suitable areas for geothermal sources (Waswa, 2017; Chan et al., 2018; Mia et al., 2014; 2018; Calderón-Chaparro et al., 2019; Ramírez-González et al., 2019). Remote sensing and geographic information system (GIS) are widely used in various stages of geothermal energy exploration and evaluation studies, such as the identification and monitoring of potential target areas (Vaughan et al., 2003, 2012*a* and *b*; Gutiérrez et al., 2012; Kruse, 2012; Giordano et al., 2013; Van der Meer et al., 2014; Wang et al., 2014; Calvin and Pace, 2016; Mia et al., 2018; Reinisch et al., 2020).

The Edremit Basin in the Biga Peninsula is a known geothermal field, and in this work, we used a multi-approach technique to analyze the surface evidence of the field (Figure 1a). The Edremit Basin and its surroundings covering an area of about 5000 km^2 are the subject of this investigation. In the research, we combined various methods that deal with geology, tectonic, hydrogeochemical, and remote sensing data. Geometric and kinematic analyses of structural characteristics are all included in the tectonic research. Remote sensing analyses comprise determination of anomalies of land surface temperature (LST) and hydrothermal alteration by using multispectral satellite images and multispectral satellite images as well as investigation of surface deformation pattern by using InSAR data.

Additionally, spatial data layers are combined, analyzed, and evaluated using GIS in order to determine the best location for geothermal potential. Hydrogeological studies consist of geochemistry of thermal and cold waters in the Edremit-Derman geothermal field. Utilizing a variety of chemical geothermometers and mineral-fluid equilibrium models, hydrogeological research aims to identify the characteristics of hydrogeochemical facies and calculate the fluid reservoir temperatures. In addition, evaluation of the stable isotope compositions (oxygen-O, hydrogen-H) of the waters revealed the origins of the compounds dissolved in the waters and to provide insight about the chemistry of the fluids in the potential geothermal areas. Tritium (T) is the radioactive isotope of hydrogen with a half-life of 12.32 years. The subsurface circulation time of the water was estimated using data from tritium isotopes. The relationship between the hydrogeochemical data and geological and remote sensing studies is examined.

The aim of this study is to investigate the geothermal energy potential of the Edremit (Balıkesir) Basin with geological, tectonic and hydrogeological studies based on remote sensing data, and to analyze and evaluate the available data in GIS application for the reconnaissance of possible geothermal target areas.

2. Geological and Hydrogeological Settings

2.1. Geological Setting

The Biga Peninsula (NW Türkiye) is located at the north of the İzmir-Ankara Suture Zone, which separates the Sakarya Zone in the north from the Anatolide-Tauride Block in the south. The region witnessed two main events: Closure of Paleo- and Neo-Tethys Oceans and it was formed as a tectonic mosaic by different continental units, representing the Sakarya Continent and oceanic assemblages of different origin and ages (Şengör and Yılmaz, 1981; Okay and Tüysüz, 1999; Bozkurt and Mittwede, 2001; Okay et al., 2008).

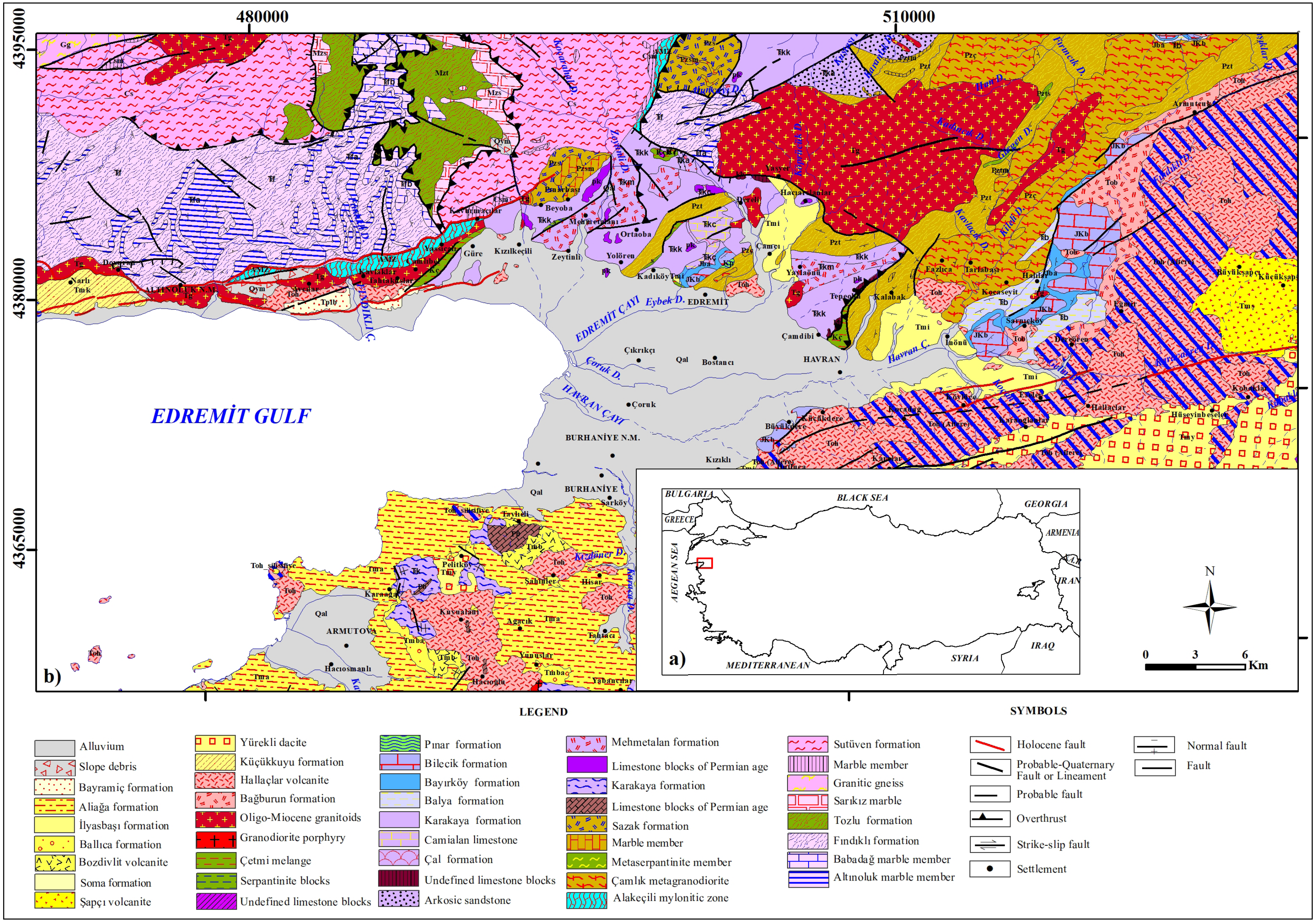

Figure 1- a. Location of Edremit Basin in Türkiye; b. Geological map of study area (Duru et al., 2004; Duru et al., 2007*a, b*; Dönmez, 2013; Emre et al., 2011).

The basement rocks in the region are quartz micaschist and minor calc-schist, metaquartzite, marble and eclogite, called as 'Çamlıca Metamorphics' and 'Kazdağı Massif' (Okay et al., 1991). The age of metamorphism is suggested as the Late Cretaceous–Early Paleocene (70–64 Ma) (Okay and Satır, 2000; Aygül et al., 2012). The Kazdağ Massif forms a structural and topographic dome of high-grade metamorphic rocks (Okay and Satır, 2000). It crops out as a tectonic window under the Karakaya Complex that includes the remnants of Paleotethys Ocean. The Complex consists of metabasic and metasedimentary rocks with Permian limestone blocks (Okay and Göncüoğlu, 2004). The cover units consist of widespread Eocene to Pleistocene volcanic and plutonic rocks, continental and shallow to deep marine sedimentary rocks (Siyako et al., 1989; Dönmez et al., 2005; Altunkaynak and Genç, 2008; Genç et al., 2012; Ilgar et al., 2012). Cenozoic magmatism is the result of northward subduction of continental slab during the closure of Neotethys Ocean (references and discussion in Okay and Satır, 2000). The subduction-related volcanic activity started in the Eocene and lasted until the Miocene producing volcanic suites ranging in composition from basalt to dacite (Bingöl et al., 1982 and 1992; Altunkaynak and Genç, 2008). Considering the literature data (Duru et al., 2007*a*, *b*; Emre et al., 2011; Dönmez, 2013; TJVT database) and field observations, a simplified geological map of the Edremit area was prepared (Figure 1b).

The geology of the region is basically dominated by two main features: (1) the widespread occurrence of Cenozoic magmatism, and (2) NE-SW striking of all geological features as a result of dextral strike-slip faulting (Beccaletto, 2003). This resulted in the development of a more complex stratigraphic succession. From bottom to top, the stratigraphic succession is briefly explained as follows: Metamorphites so called Çetmi mélange and Kazdağ metamorphites form the basement rocks (Figure 2). The Cretaceous Çetmi mélange consists of ophiolitic units and various rocks. It is composed of tectonic slices and/or olistostromes. The stratigraphic position and fossil content of the unit indicate that the mélange was emplaced in the region before the Maastrichtian (Okay et al., 1990 and 1991; Duru et al., 2007*a*). The Kazdağ metamorphics are composed of the Altınoluk marble member, Fındıklı formation (alternations of amphibolite gneiss, marble and amphibolite), Babadağ marble member, the Tozlu formation (ophiolitic rocks), Sarıkız marble and the Sutüven formation (gneiss, migmatite, marble and granitic gneisses). These metamorphics are cut by Oligo-Miocene granitoids. Dating by ^{207}Pb/^{206}Pb method indicates that the Kazdağ metamorphites are Late Carboniferous in age (Okay et al., 1996). However, 233±24 Ma age obtained from K/Ar method shows that the age of the unit is late Early Triassic-early Late Triassic (Bingöl, 1969 and 1971). The Carboniferous-Devonian Kalabak group overlying the Kazdağ metamorphics with a tectonic contact consists of low-grade metamorphics (Duru et al., 2007*b*). It contains the Torasan formation represented by phyllites, schists, metavolcanites and marbles. The Sazak formation (metatuff, metavolcanite, phyllite, schist, metabasite, marble and recrystallized limestone) and the Çamlık metagranodiorite (Devonian-Carboniferous) cut by several young granites and aplitic dykes. The Karakaya complex unconformably overlies the Kalabak group with a tectonic relation (Duru et al., 2007*a*, 2007*b*). The basal contact of the complex, which is considered to be Triassic in age, is mostly defined as tectonic.

The Balya formation, Late Triassic sandstone and Halobian shales, forming the cover units of the Sakarya Zone, unconformably overlie the units of the Kalabak group. The Bayırköy formation, Early Jurassic conglomerate, sandstone, siltstone, claystone and clayey limestone set above the Balya formation. Bilecik formation (Callovian-Hautrivian limestones) is widely seen in the Sakarya Zone. The Pınar formation of Hautrivian-Albian age is made up of hemipelagic, micritic limestone and claystone alternation. Most of basin deposits are found on top of the Sakarya Zone. They start with andesitic lava, ignimbrite, agglomerate and volcanoclastics of the Bağburun formation which is the product of volcanism that continued until the Late Oligocene-Early Miocene (Dönmez et al., 2005). Altered volcanic rocks of the Hallaçlar volcanite are observed at the upper part of the Bağburun formation. Shallow intrusions generally of granodioritic composition emplaced in the region in the Oligocene-Late Miocene interval. The Küçükkuyu formation, which is composed of Miocene bituminous shale, tuff, mudstone, sandstone, conglomerate and limestones, unconformably overlies the Hallaçlar volcanics. The

Early Miocene dacite, rhyolite and rhyodacites cut the Hallaçlar volcanite. They are also unconformably overlain by the Late Miocene Aliağa formation consisting of conglomerate, sandstone, claystone, tuff, tuffite, claystone and lacustrine limestone. The Early Miocene Şapçı volcanite, which is composed of andesite and pyroclastics unconformably overlies the Yürekli dacite. The conglomerate and sandstone of Middle Miocene Ballıca formation unconformably overlie the Middle Miocene Bozdivlit volcanite, which consists of lavas of basalt-andesite composition. The unit is transitional to the lacustrine sandstone, claystone, tuff, tuffite and limestones of the Aliağa formation. The Late Miocene İlyasbaşı formation, which is composed of marl, limestone, mudstone, tuff, sandstone and conglomerate, covers the Early Miocene units. The Bayramiç formation that comprises the Plio-Quaternary fluvial deposits and Quaternary alluvial deposits unconformably sets above all these units.

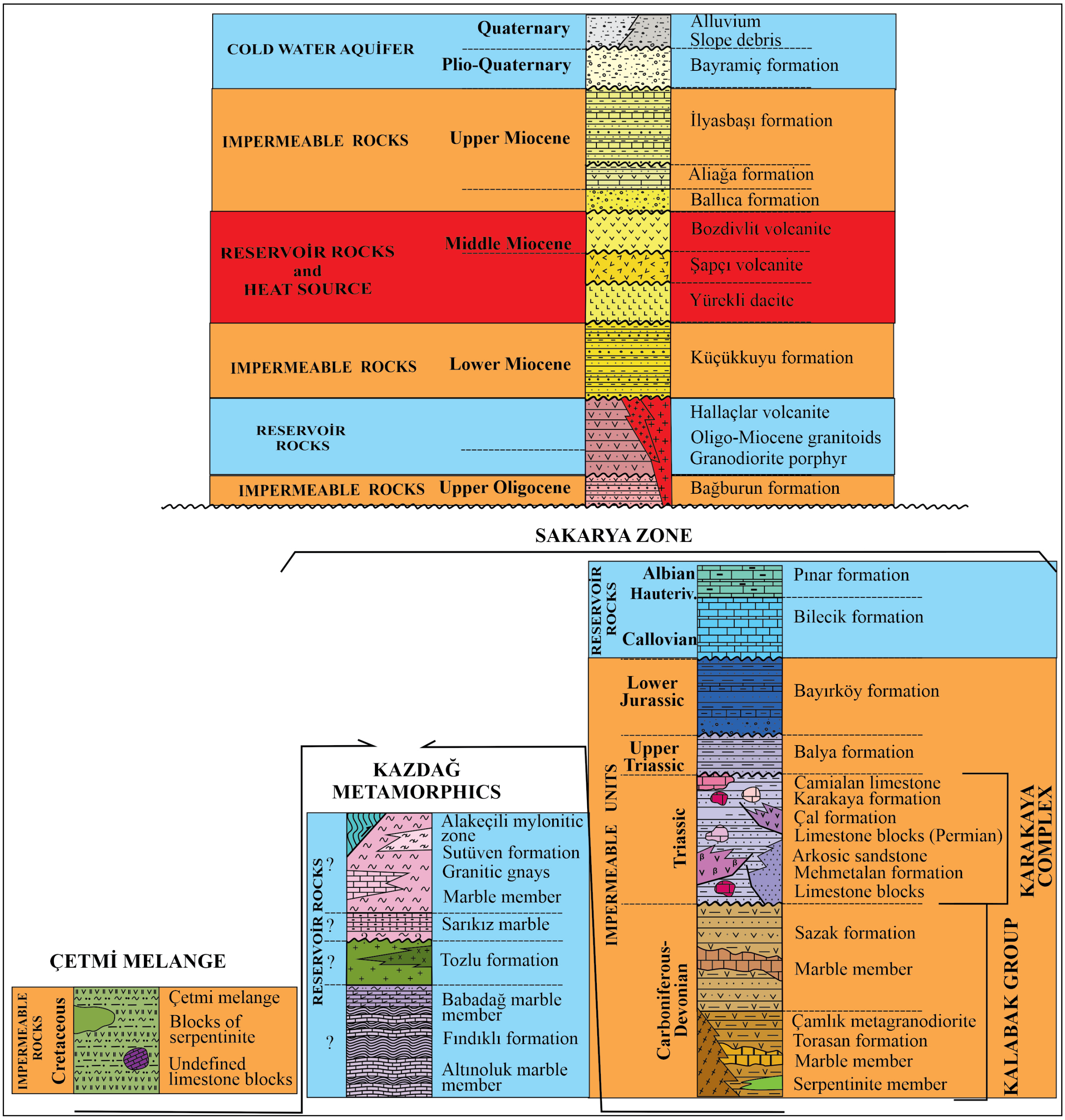

Figure 2- Stratigraphic section of the Edremit Basin (modified from Duru et al., 2004, 2007*a*, *b;* Dönmez, 2013).

2.2. Hydrogeological Setting

Reservoir rocks that are composed of porous and permeable units make up the most important part of a geothermal system. They have gained secondary porosity by tectonic and lithological effects. In the Edremit-Güre area, marble levels of the Kazdağı Massif, Jurassic limestones, conglomerates within the Paleocene-Eocene sediments, sandstone, fractured volcanic rocks and pebbly sandy Miocene sediments comprise the reservoir rocks (Sarp et al., 1998). Avşar et al. (2013) reported the presence of two different aquifers in the Edremit geothermal field. They stated that the shallow aquifer is comprised of Quaternary and Plio-Quaternary unconsolidated sandstone, conglomerate and mudstone units. The units consisting of agglomerate and conglomerate over the Kazdağ Metamorphites are regarded as the second aquifer. According to Yalçın (2007), the Upper Jurassic-Lower Cretaceous limestone acts as a reservoir rock while the Karakaya Complex is of impermeable character. However, some of the wells receive thermal water from the Karakaya Complex. The Karakaya complex is impermeable and the fractured character as a result of tectonism increases the water-transfer capacity of the unit. Magmatism represented by Miocene volcanics and granitic rocks (Karacık and Yılmaz, 1998) constitutes the heat source for the geothermal system. The cover rock is another important component of the geothermal system, which is necessary for the storage of thermal fluid. In the Edremit basin, clayey, silty layers of sedimentary rocks, tuffs and volcanic rocks are the major cap rocks.

Edremit field is one of the important geothermal fields of Western Anatolia. In this field, almost 50 wells have been drilled by both private firms and government institutions (Erzenoğlu, 1985; Güner et al., 1994; Sarp et al., 1998; Ölmez et al., 2001; Dilemre et al., 2006; Avşar, 2011; Avşar et al., 2013). The depths of the wells are between 20-1350 m and the temperatures of waters from these wells varies between 21-65°C. Sarp et al. (1998) drilled 4 gradient wells in the Edremit field in order to determine the geothermal gradient and the locations of the deep production wells. The depths of the gradient wells vary from 122 to 300 m. As a result of the temperature measurements in the gradient wells, the geothermal gradient was calculated as 0.29°C/10m-1.28°C/10m (Sarp et al., 1998). The highest gradient value was obtained in the well drilled in granitoids that is the reservoir rock. Demet-1, ED-1, ED-2, ED-3, Güre-1, Güre-2 and BGK-2011/19 production wells were drilled by General Directorate Mineral Research and Exploration (Table 1). The drilled at a depth of 400 m and the bottom temperature of this well was determined 53°C. The water produced from Demet-1 well has a flow rate of 1.5 l/s and a temperature of 40°C (Erzenoğlu, 1985). The ED-2 well is at a depth of 495.5 m and the bottom temperature of the well is

Table 1- Temperature, depth and production information of some of the wells in the Edremit basin.

Well name	Depth (m)	Temperature (°C)	Flow rate (l/s)	Coordinates			Reference
				Y	X	Z (m)	
Demet-1	400	40	1.5	-	-	-	Erzenoğlu (1985)
ED-1	189.5	60	75	4380395	503642	25	Ölmez et al. (2001)
ED-2	496.5	47	2	4380293	504014	27	Ölmez et al. (2001)
ED-3	495	59	18	4380335	03710	24	Ölmez et al. (2001)
EDJ-2	300	58	75	4380049	503916	24	Avşar et al. (2013)
EDJ-3	266	59	50	4380252	503634	21	Avşar et al. (2013)
EDJ-4	296	50	86	4380136	503458	19	Avşar et al. (2013)
Güre-1	196.20	55	6,5	490125	482300	10	Didik et al. (1994)
Güre-2	153.70	33	7	490300	482850	15	Didik et al. (1994)
İGJ-1	167	64	32	490224	4832366	-	Dilemre et al. (2006)
İGJ-2	250	56,3	50	490060	4382174	-	Dilemre et al. (2006)
İGJ-3	206	67	40	490215	4382392	-	Dilemre et al. (2006)
İGJ-3	250	67	40	490332	4382392	-	Dilemre et al. (2006)
İGJD-1	1350	96	30	490316	4382228	12	Dilemre et al. (2006)
BGK-2011/09	750	33,3	30	489133	4363577		Bulut et al. (2018)

55.4°C. The gradient value calculated for this well is 0.26°C/10 m. The thermal water was obtained from the well at a temperature of 47°C and a flow rate of 2 l/s (Ölmez et al., 2001). The thermal water produced from the wells is used for heating of residences, thermal facilities and greenhouse and also for thermal tourism.

3. Methods

In this study, geothermal energy potential of the Edremit Basin is investigated using remote sensing method (LST, hydrothermal alteration and InSAR) and geological, tectonic and hydrogeological data. All the data were evaluated with a GIS application. The study was carried out in three stages (Figure 3).

The first stage comprises processing of the satellite images (anomalies maps of LST, hydrothermal alteration as well as InSAR analysis). During the field work, data were collected from the ground truth, faults, and various types of rock and sampling of thermal and cold waters. This is followed by the construction of geological and tectonic framework based on the geological map of the area which is mainly related to literature data. Descriptions of the units in the litostratigraphic section and faulting mechanism were obtained from previous studies and recent earthquakes data. The last step includes GIS study to combine, analyze and evaluate all the spatial data layer.

Three groups of analysis were carried out within the scope of remote sensing studies. The first is the preparation of surface temperature (LST) map from thermal bands of satellite data that is one of the most important remote sensing works widely used in the geothermal energy exploration. The second is the determination of hydrothermal alteration anomaly areas and the third one is defining the surface deformations by interferometric analysis of SAR images.

Field study is the ground truth step of all combined data. Geological, stratigraphical and structural mapping were checked during field study. Stratigraphical features are the key point for the heat source and reservoir rocks of thermal springs. Collection of field data includes measurements of striations and fault plane. A total of 133 fault plane/striations were measured at 19 different sites. Statistical analyses of faults and joints are processed in the lower hemisphere projection using the software employed for stress inversion of fault slip data (Angelier, 1979). During the fieldwork, thermal and cold water samples were collected from the wells and springs. Some physical

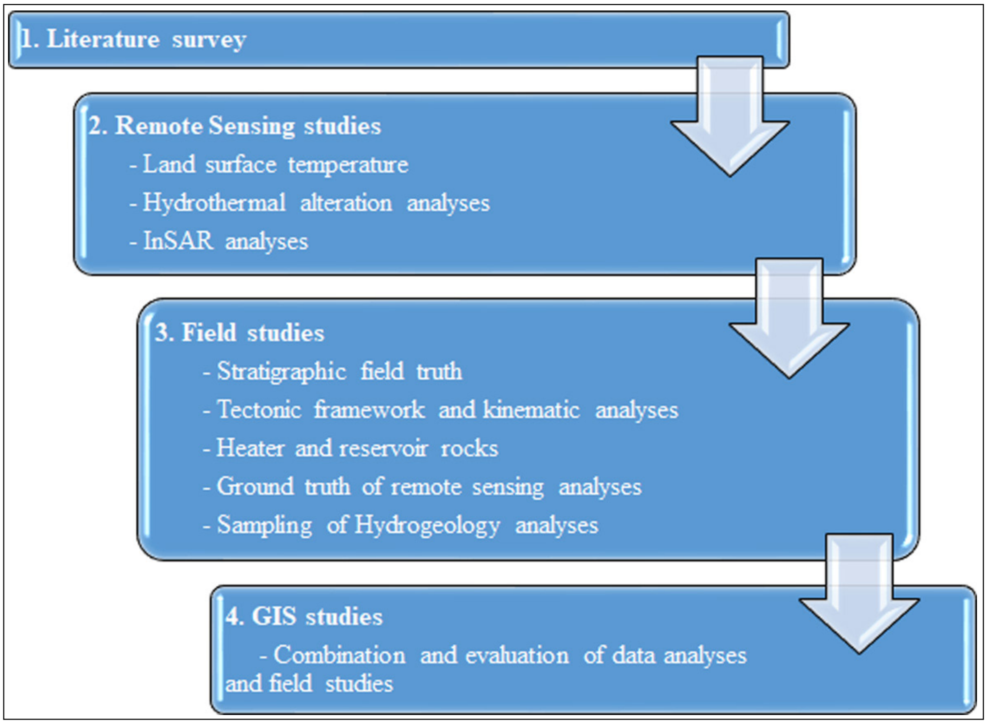

Figure 3- General methodological flowchart.

parameters were recorded during the collection of water samples (Table 2). The thermal water ES-1 was taken from the deepest well (1350 m) with the highest temperature at the northwest of field (in Güre). The ES-2 sample was collected from a well drilled in alluvium at a depth of 64 m (in Havran). The ES-3 sample that has a temperature of 32 °C was taken from a well drilled that has a depth of 640 m in the south of the field. The E-4 sample was taken from a low-elevation stream. The sample E-5 is a cold water spring that discharges from high elevations. Their temperature was measured at the sampling site. From each spring, three samples are collected and 0.2 ml of HNO_3 was added to one of the samples to prevent precipitation of cations. Another batch was collected for isotope ($\delta^{18}O$, $\delta^{2}H$, ^{3}H) analysis. Chemical analysis of the waters was carried out at the laboratories of the General Directorate of Mineral Research and Exploration with the standard methods. The cations (Ca^{+}, Mg^{2+}, Na^{+}, K^{+}) and SiO_2 concentrations were determined by Inductively Coupled Plasma Optical Emission Spectrometry (ICP-OES). This method is also used in As, B and Li analysis. Titration method is used in HCO_3^{-} and CO_3^{2-} analysis. SO_4^{2-}, Cl^{-} and F^{-} analyses were made using the Ion Chromatography Method (ICM). $\delta^{18}O$ and δD (reported as V-SMOW) analyses were performed with laser spectrometry and tritium (^{3}H) analyses are made with a liquid count scintillation system at the General Directorate of State Hydraulic Works TAKK Laboratories. Lastly, the combination and evaluation of all data are presented on a final map constructed by GIS application.

4. Field Observations and Analysis

Four main study package have been applied in the content. Structural geology, remote sensing (calculation of surface temperature, determination of hydrothermal alteration, InSAR analysis), water chemistry and isotopic data (geochemical characteristics of Edremit and Güre waters, isotope geochemistry, geothermometer applications) and GIS application. They all were investigated and applied separately and then combined in GIS layers.

4.1. Structural Geology and Fault Kinematics from Field Study

The Edremit Basin located in the Biga Peninsula is a tectonically active area controlled by a normal faulting mechanism with right lateral component dominantly. It is formed in association with the North Anatolian Fault System (NAFS), Aegean Extensional System (AES) and the motion of plates around Türkiye (McKenzie, 1972; Jackson and McKenzie, 1988; Kaya, 1978; Gessner et al., 2013; Jolivet et al., 2013; Özkaymak et al., 2013; Uzel et al., 2013; Gürer et al., 2016; Gürer, 2023). The configuration implies that the peninsula moves to the west and southwest with a velocity of 2–3 cm/year (McClusky et al., 2000; Straub et al., 1997; Aktuğ et al., 2009). There are various mechanisms for the origin of basin: (a) strike-slip faulting associated with the NAFS (e.g. Okay and Satır, 2000), (b) normal faulting controlled by AES (Kurtuluş et al., 2009), and (c) coupled effects of both NAFS and AES (e.g. Yılmaz and Karacık, 2001; Boztepe-Güney et al., 2001; Gürer et al., 2016). Evolution of a basin has a great control on geothermal capacity. Not only the displacements along the active faults but also paleo structures act as passage for groundwater circulation. For this reason, the map of structural lineaments recorded during the field study and obtained from the literature are presented in Figure 4. The results show the existence of a dense

Table 2- Coordinates and physical parameters of the sampled waters in study field.

Sample No	Well Name	Coordinates			Well Depth (m)	T* (°C)	pH	EC* µS/cm	References
		Y	X	Z					
ES-1	İGJD-1	490316	4382228	12	1350	86	8.5	1211	This study
ES-2	Altın Tohumcu	503078	4379448	22	64	32	7.4	1132	This study
ES-3	Gömeç	488235	4362501	52	640	32	8.1	1855	This study
ES-4	Hasanboğuldu	492945	4388545	259	Spring	15	8.1	229	This study
ES-5	Çamtepe Village	504970	4367950	487	Spring	19	7.4	449	This study
EDR-1*	EDR-1	490103	4381735	7	Spring	60	8.2	945	Yalçın, 2007
ED-3*	ED-3	503639	4380394	22	495	62	7.7	1060	Avşar et al., 2013
IGJ-2*	IGJ-2	490060	4382174	9	250	46.2	8.6	864	Kaçar et al., 2017

*: These samples are included here for comparison with samples taken in this study.

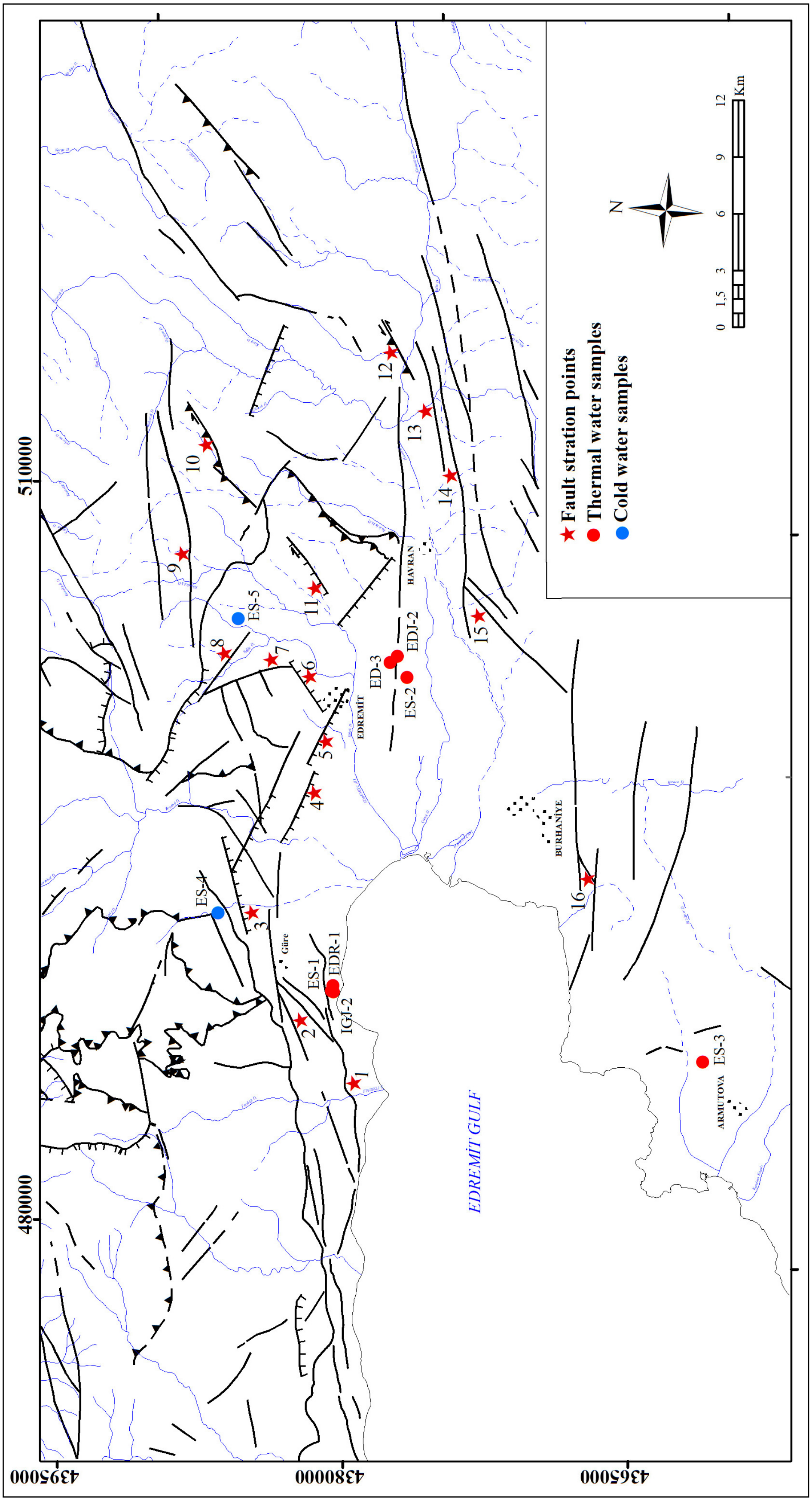

Figure 4- Main structures around the Edremit Basin; striation and water sample points (Faults and active faults: Duru et al., 2004; Duru et al., 2007*a*, *b*; Dönmez, 2013; Emre and Doğan, 2010; Emre et al., 2011; faults determined during the field study).

network of fractures that would affect the geothermal area in the Edremit Basin. Faults are crucial structures in groundwater moving to the surface. These structures' ability to convey fluid is directly impacted by the stress distribution under which they are created. Because of this, the development processes of the faults are identified, and crucial information on their lengths and groundwater capacities is gained based on the kinematic analysis of the fault striations taken over the fault surfaces. According to the older and current tectonic regimes, regional evaluation was made using the fault slip data. The locations of the places were marked with asterisks in Figure 4.

Kinematic analyses of fault striations are used to determine dominant stress directions operated on the faults. There is different software for the paleostress analysis based on the stress distribution. In this study, measured data obtained from the fault surfaces were analyzed according to methods proposed by Angelier (1984), T-TECTO. The data set was processed by the Direct Inversion Method (INVD) assuming that the slip is parallel to the calculated maximum shear stress. According to this assumption, the ratio of the principal stress differences is $R = (\sigma 2 - \sigma 3) / (\sigma 1 - \sigma 3)$. R has a range between 0 and 1, and when R goes to 0, faulting mechanism is dominated by $\sigma 1$ as vertical (extensional), R closes to 1, faulting mechanism is dominated by $\sigma 3$ as vertical (compressional) and in between $\sigma 2$ is dominant and strike slip motion appears (Angelier, 1984). To analyze the striations for the stress distributions, we measured kinematic data along the fault planes, which are located particularly along the margin faults in the Edremit Basin (Figure 5). A total of 133 measurements from 19 different locations were used for stress configurations (Figure 6).

Structural geology should be the prime strategy for geothermal exploration studies. From this point of view, marginal faults in the Edremit Basin and some lineaments around the basin were measured and analyzed. Striations indicate that different types

Figure 5- Some field photographs and striations from fault surfaces; a) station 1, b) station 3, c) station 5, d) station 6, e) station 8 and f) field photographs from station 16 in Figure 5.

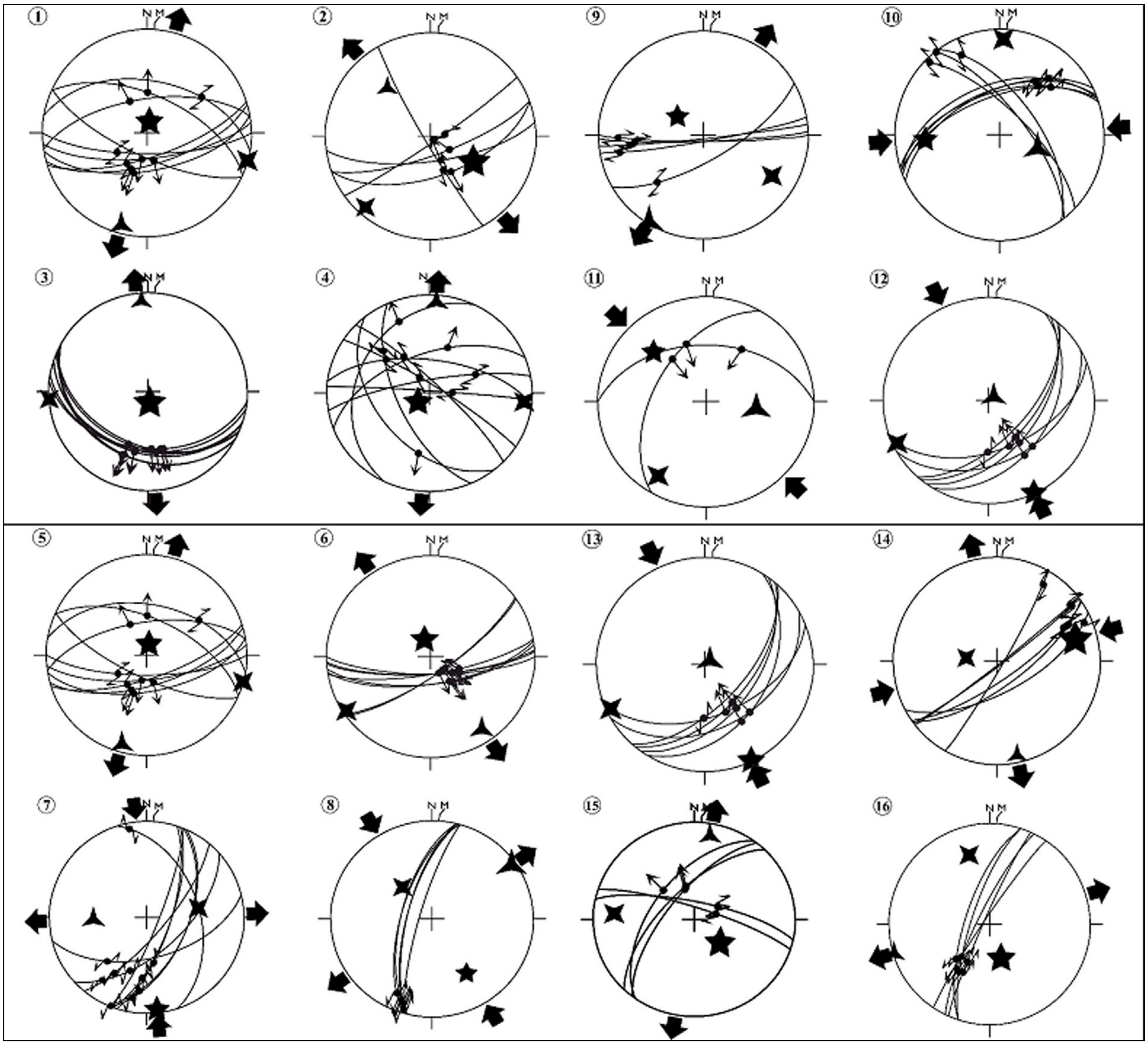

Figure 6- Kinematic analyses of fault striations measured at locations given in Figure 4.

of faulting mechanisms are effective in the area. Each point (1-16) and their kinematic results are presented in Figure 7 and according to the main faulting mechanism N-S extensional stress distribution is dominant around the Edremit Basin. In this case, the most probable faulting direction is around E-W and striking structures have normal motion such as the faults with measurement numbers of 1, 2, 3, 4, 5, 6, 9, 15 and 16 (Figures 5 and 6). On the other hand, 7, 8, 10, 11, 12, 13 and 14 indicate strike slip and reverse faulting mechanisms. Measurements 12 and 13 have reverse mechanism that are probably inherited from paleotectonic period.

4.2. Remote Sensing Studies

In this study, thermal bands of day/night time ASTER, Landsat 8 and Landsat 7 ETM+ satellite images were used to calculate LST values (Table 3). Two Landsat 8 TIRS (Thermal Infrared Sensor) images (acquisition date of 02.09.2017) with path-row number 181/033 were used. Two Landsat 7 ETM+ images with the same path-row number as Landsat 8 were obtained (10.09.2017). The acquisition date of two ASTER daytime thermal images is 20.09.2000 and the acquisition date of two ASTER nighttime thermal images is 27.06.2013. ASTER day and night times images are ASTER Surface Kinetic Temperature

Table 3- Satellite images used in this study.

Thermal Analysis				**Alteration**	**InSAR Analysis**
Landsat 8 OLI	**Landsat 7 ETM+**	**ASTER-day**	**ASTER-night**	**ASTER VNIR-SWIR**	**ALOS Palsar-1**
02.09.2017	10.09.2017	20.09.2000	27.06.2013	02.11.2004	04.01.2007-15.01.2011 (19 images)

(AST_08) data generated using the Temperature Emissivity Separation Algorithm (TES) (Gillespie et al., 1998). These data are from NASA Earth Science Data (NASA, 2019) while Landsat 8 TIRS and Landsat 7 ETM+ images were obtained from USGS (USGS, 2019).

Areas for the hydrothermal alteration anomalies associated with geothermal systems were determined applying band ratio method to spectral bands in the visible-near infrared (VNIR) (0.52-0.85 µm) and short-wave infrared (SWIR) (1.600-2.430 µm) region of the ASTER image~~s~~ (01.11.2004). The multi-temporal InSAR (MTInSAR) analysis of ALOS Palsar-1 (L-band) SAR images were used to define the surface deformations (subsidence, uplift) in the basin. In the MTInSAR analysis, ascending 19 ALOS Palsar-1 images taken between 04.01.2007 and 15.01.2011 were used (Table 4). ALOS Palsar-1 images were analyzed by applying the "Small Baseline Subset Interferometry (Small BASeline Subset-SBAS)" technique, which is one of the Multi-temporal InSAR (MTInSAR) methods.

Table 4- Acquisition dates of ALOS Palsar-1 images.

ALOS Palsar-1			
4.01.2007	9.10.2008	12.10.2009	30.05.2010
7.07.2007	9.01.2009	27.11.2009	15.07.2010
7.10.2007	24.02.2009	12.01.2010	30.08.2010
7.01.2008	12.07.2009	27.02.2010	15.01.2011
24.05.2008	27.08.2009	14.04.2010	

4.2.1. Calculation of Surface Temperature Values with ASTER Day/Night Times Thermal Images

Thermal infrared remote sensing analysis has been extensively used for the last years to identify surface temperature anomalies related with geothermal activity (Allis et al., 1999; Hook et al., 1999; Ayenew, 2001; Pieri and Abrams, 2005; Vaughan et al., 2012*a* and *b*; Haselwimmer and Prakash, 2013; Wessels et al., 2013). Satellite data such as MODIS, ASTER, Landsat 8 TIRS and Landsat 7 ETM+ and thermal cameras are widely used in this context. In order to obtain surface temperature values from the thermal bands of satellite images, many algorithms such as Radiative Transfer Equation (RTE), Single-Channel (SC), Split-Window (SW), temperature and emissivity separation (TES) have been developed (Gillespie et al., 1998; Qin et al., 2011; Li et al., 2013; Jiménez-Muñoz and Sobrino, 2003; Jiménez-Muñoz et al., 2014; Yu et al., 2014). ASTER day-time and night-time surface temperature maps were produced from AST08 surface kinetic temperature data. A scaling factor of 0.1 was applied to the surface kinetic temperature data of ASTER AST08 and the temperature values were converted to degrees Celsius. Then, the ASTER temperature maps of the study areas were prepared. Band 10 of Landsat 8 TIRS images and band 6 of Landsat 7 ETM+ images were used to calculate LST values. The procedures given the flowchart in Figure 7 were applied to compute the surface temperature values from the thermal bands of Landsat 8 TIRS and Landsat 7 ETM+ images. Landsat 8 TIRS and Landsat 7 ETM+ thermal bands were atmospherically corrected using parameters estimated by the atmospheric correction parameter calculator web tool (Barsi et al., 2003 and 2005). The emissivity (ε) values of Landsat 8 TIRS band 10 and Landsat 7 ETM+ band 6 are calculated using the NDVI Thresholds Method ($\mathrm{NDVI}^{\mathrm{THM}}$) (Sobrino et al., 2004; 2008) modified the existing land surface emissivity (LSE) calculation method based on Normalized Difference Vegetation Index (NDVI) (Van de Griend and Owe, 1993; Valor and Caselles, 1996). LST values were calculated using the single band algorithm generalized by Artis and Carnahan (1982) based on the Planck function using a single band (Equation 1).

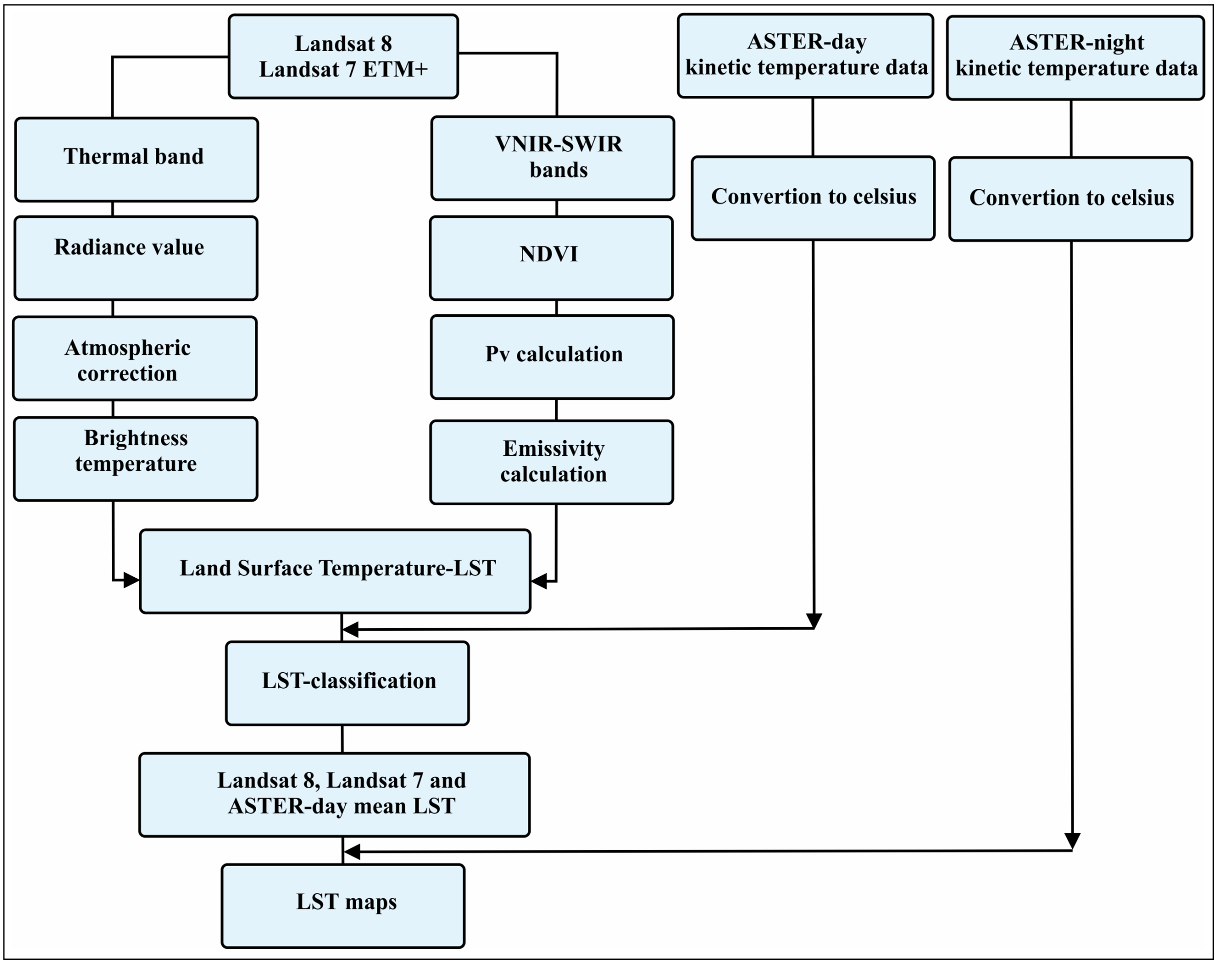

Figure 7- Flowchart of LST calculations.

$$T_s = \frac{BT}{\left\{1+\left[\frac{\lambda \cdot BT}{\rho}\right]\cdot ln\varepsilon\right\}}$$ ……..............…..Equation 1

Ts : land surface temperature (K)

BT: at-sensor brightness temperature (K)

λ : wavelength of the emitted radiance

● : h * c/s=1.438 x 10^{-2} m K

h : Planck’s constant (6.626 x – 34 Js)

S : Boltzmann Constant (1.38 x – 23 J/K)

c : Velocity of light (2.998 x – 8 m/s)

ε : spectral emissivity

In order to increase the accuracy of LST results obtained from satellite data, approximately 10 highest temperature values on ASTER-daytime, Landsat 8 TIRS and Landsat 7 ETM+ LST maps were reclassified for each map. Then, the average daytime LST map was produced by taking the arithmetic average of these values (Figure 8).

4.2.2. Determination of Hydrothermal Alteration Anomaly Areas

In a geothermal system, changes known as alteration occur in the mineralogy, texture and chemistry of the rocks by the effect of thermal water, steam and fumaroles (Van der Meer et al., 2014). These changes are the indicators of underground geothermal systems on the ground surface. At certain temperatures, clay (kaolinite, illite), sulfate (alunite, gypsum), carbonate (calcite) and silica (opal, chalcedony) minerals are formed (Calvin et al., 2015). Therefore, mapping of hydrothermal alteration anomalies and identifying these minerals and/or mineral groups are important in terms of limiting the possible target areas (prospect

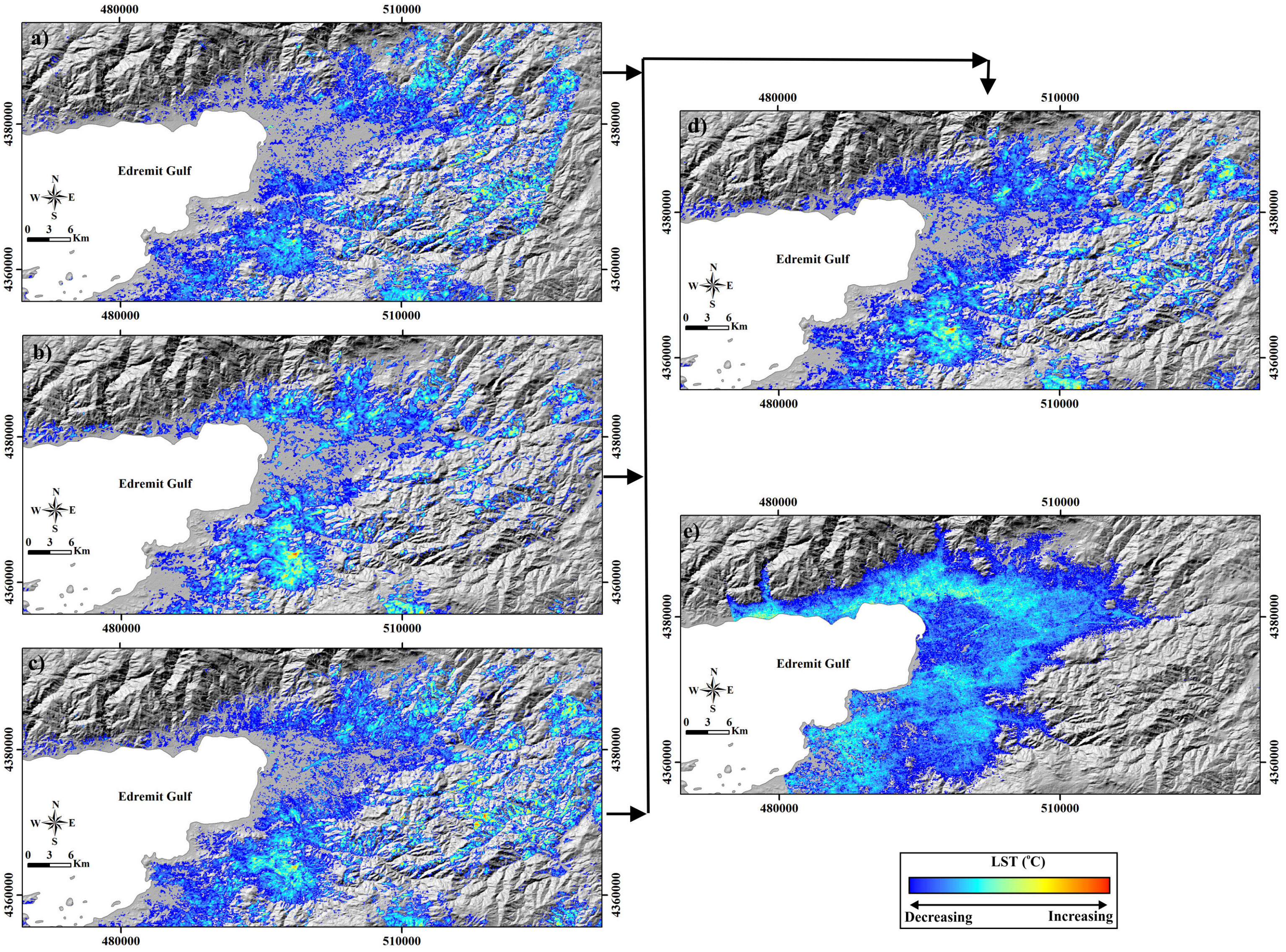

Figure 8- LST maps calculated from a) ASTER-daytime, b) Landsat 8 TIRS, c) Landsat 7 ETM+, d) average daytime and e) ASTER-nighttime (Approximately highest 10°C of temperatures values shown).

areas) for detailed studies in the early stages of geothermal exploration.

In the VNIR-SWIR region (0.4-2.5 μm wavelength), ASTER images have spectral bands corresponding to the diagnostic absorption features such as Fe^{+3}, Fe^{+2}, Al-OH, Fe-OH, Mg-OH, Si-OH and CO_3. Mineral and/or mineral groups can be determined using these descriptive absorption properties (Rowan and Mars, 2003; Rowan et al., 2003; Kalinowski and Oliver, 2004; Hewson et al., 2005). In order to define the anomaly areas of hydrothermal alteration in the Edremit basin, the VNIR-SWIR bands of the ASTER image were analyzed applying the band ratio technique. The bands in the VNIR-SWIR regions of the ASTER Level 1T image dated 02.11.2004 were combined and then the relevant part of the study area was obtained by cutting from the whole image. Afterwards, vegetation and water areas were masked and dark area subtraction (Lpath remove) was applied to image. With the band ratio analysis of the ASTER image, ironoxide/hydroxide minerals (hematite, goethite), Al-OH containing minerals such as clay minerals (illite, kaolinite vb.), alunite/kaolinite minerals, silica minerals (opal), Mg-OH minerals (chlorite, epidote) and $CaCO_3$ minerals (carbonate minerals) were mapped (Table 5 and Figure 9).

Table 5- Band ratio applied to ASTER image and mineral/mineral groups.

Mineral and/or minerals	Band Ratio
Ironoxide/hydroxide (hematite, goethite)	2/1
Al-OH-containing minerals (clay minerals)	4/6
Alunite/kaolinite minerals	4/5
Silica (opal)	4+5/6+7
Mg-OH -containing minerals (chloride, epidote) and $CaCO_3$-containing minerals (carbonate minerals)	7+9/8

4.2.3. InSAR Analyses

Interferometric analyses (InSAR) were carried out in order to investigate the surface deformations such

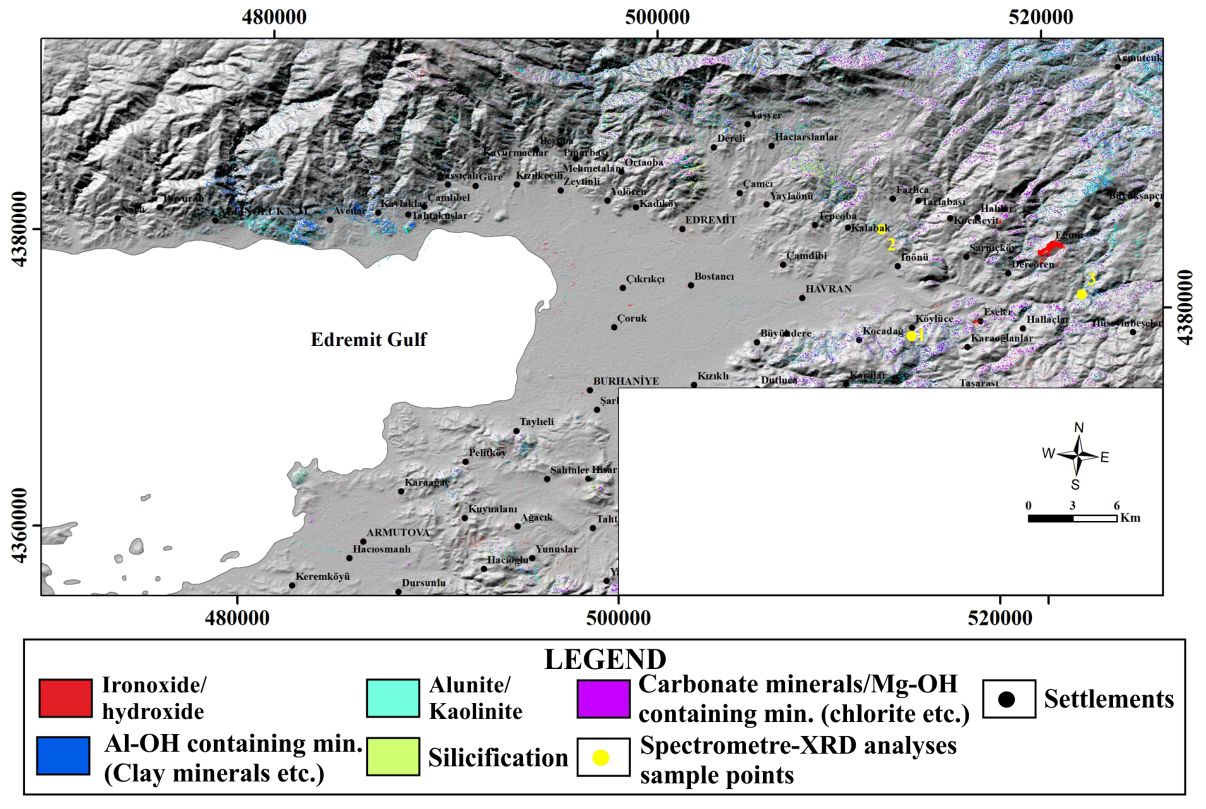

Figure 9- Hydrothermal alteration anomaly areas determined by ASTER band ratio analysis.

as subsidence, uplift etc. In this context, 19 ALOS Palsar-1 images were analyzed using SBAS method which is one of the Multi-temporal InSAR (MTInSAR) analysis techniques (Berardino et al., 2002). ALOS Palsar-1 images cover a time interval of 1518 days between the dates of 04.01.2007 and 15.01.2011 (Figure 10). By creating 132 interferometric pairs, ALOS Palsar-1 SBAS analysis was carried out.

As a result of ALOS Palsar-1 SBAS analysis, the amount of line of sight (LOS) surface deformations (mm) and the velocity rate (mm/year) were obtained. Results of analysis indicate that the LOS surface deformations (collapse-rise, etc.) are between about < -165 and >180 mm and the LOS velocity rates range from about < -26 to > 27 mm/year (Figure 11).

4.3. Water Chemistry and Isotopic Data

Major anion-cation and trace element concentrations of thermal and mineral waters sampled in the Edremit and Güre geothermal areas are given in Table 6. The analysis results were used to determine the chemical properties, reservoir temperatures, and mineral saturation of the waters. The results of isotope compositions ($\delta^{18}O$, δD and tritium) of the waters are presented in Table 7. The isotope results provide information on the water-rock interaction and the source of solutes in waters.

4.3.1. Geochemical Characteristics of Edremit and Güre Waters

The pH and temperature of the Edremit and Güre waters are 7.4-8.5 and 32-86°C, respectively. The measured electrical conductivity values are between 229-1855 µS/cm, and the total dissolved solid (TDS) contents range from 137 to 1341 mg/l.

The hydrogeochemical facies of the waters are defined by the dominant cation–anion pairs (concentrations in meq/l %). The Schoeller diagram shows that the thermal waters have the same origin and are mostly dominated by Na+K and SO_4 concentrations (Table 6 and Figure 12). However, cold waters (samples ES-4 and ES-5) are represented by Ca^{+2} and HCO_3^-. In the Piper diagram (Piper, 1944), the Edremit-Güre waters plot in two separate areas (Figure 13). The thermal waters fall into the $NaSO_4$ waters field, indicating a deep circulation and the cold-water samples plot into the field of $CaCO_3$ dominated waters.

Bor (B) concentration varies between 0.9-3 mg/l in thermal waters. B, due to its high solubility and volatility under high temperature, easily enters the composition of water. Tourmaline in igneous rocks is the source of boron. The presence of boron is an indication that water is interacting with granitic rocks. Brom (Br) is rare in geothermal waters. It is more common in seawater-fed or evaporitic waters. Br values in Edremit basin are quite low. Although arsenic is a mobile element, its solubility is low. As values in thermal waters in Edremit Field are quite low. It is thought that it is added to the composition of the water because of contact with the metal sulfides in the rocks through which the water passes.

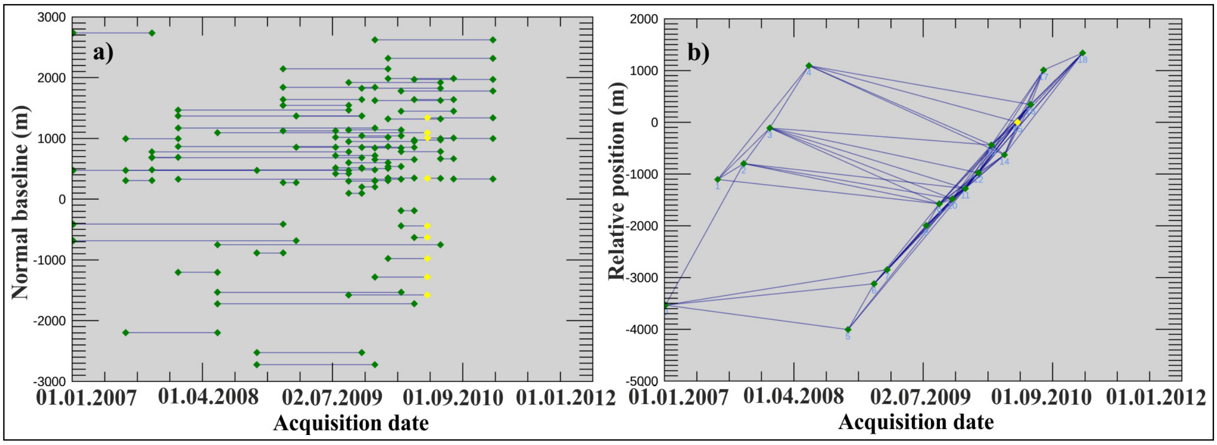

Figure 10- Plots of interferometric SAR image pairs versus time a) normal baseline and b) relative position graphs.

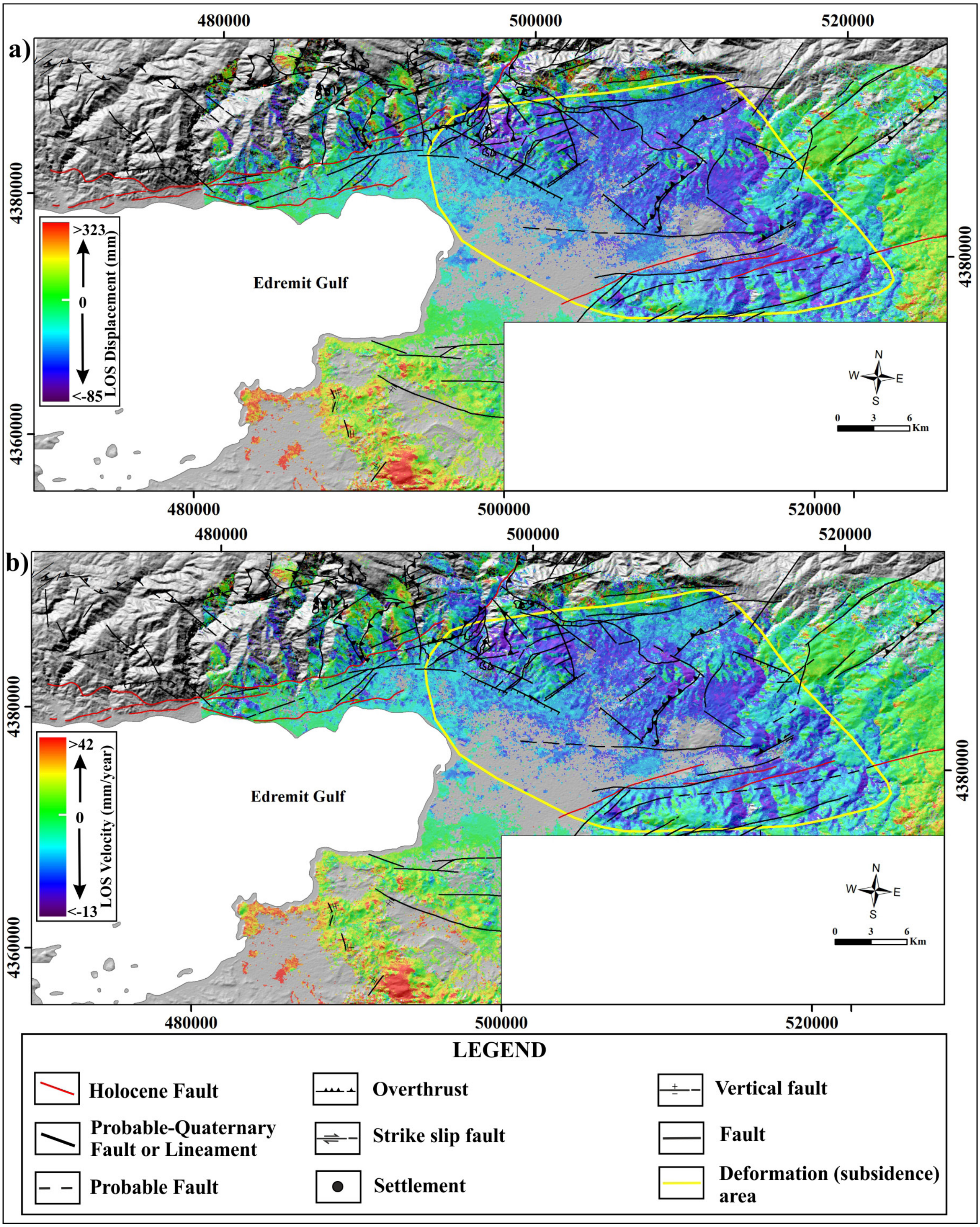

Figure 11- The result of ALOS Palsar-1 SBAS analysis a) LOS deformation (mm) amount, b) LOS velocity rates (mm/year) (faults and active faults: Duru et al., 2004; Duru et al., 2007*a, b*; Dönmez, 2013; Emre et al., 2011; faults determined during the field study).

Table 6- Results of chemical compositions of thermal and mineral waters from the study area.

Sample No	T* (°C)	pH	EC µS/cm	Ca^{+2}	Mg^{+2}	Na^{+}	K^{+}	Cl^{-}	SO_4^{-2}	HCO_3^{-}	CO_3^{-2}	SiO_2	F^{-}	Br^{-}	B	As	Li	TDS	Water type (IAH)
ES-1	86	8.5	1211	23.7	<0.1	292	8.3	64.9	499	40.2	21.4	78.9	5.2	0.2	3	0.04	0.25	914	Na+K-SO_4
ES-2	32	7.4	1132	96.8	7.2	203	3.6	18.24	411	255	<10	33.17	1.7	0.2	0.9	<0.01	0.15	891	Na+K-SO_4-HCO_3
ES-3	32	8.1	1855	3.4	2.8	572	4.9	85	123	1127	44	32.9	1	0.2	1.5	0.01	0.18	1341	Na+K-HCO_3-SO_4
EDR-1[a]	60	8.2	945	23.8	0.6	276.3	5.9	59	506	61	<10	58.9	7.4	0.014	2.8	0.009	0.27	-	Na+K-SO_4
ED-3[b]	62	7.7	1060	25	0.2	193	3.4	48	360	54	-	32	-	-	1.6	-	-	-	Na+K-SO_4
EDJ-2[b]	58	7.6	1200	31	0.1	217	5.1	57	420	44	-	50	-	-	1.6	-	-	-	Na+K-SO_4
IGJ-2[c]	46.2	8.6	865.7	9.10	0.1	173	3.80	39	270	38.7	-	-	-	-	-	-	-	-	Na+K-SO_4
ES-4	15	8.1	229	44.1	8	4.8	<1	3.6	3.8	107	29.3	10.05	<0.1	<0.1	<0.1	<0.01	0.04	137	Ca-Mg-HCO_3
ES-5	19	7.4	449	73.8	8	32	1.3	20.7	6.4	326	<10	32.95	<0.1	<0.1	<0.1	<0.01	0.05	291	Ca-Mg-HCO_3

* On-site (well-head and spring) measurements. Cation, anion and trace element concentrations are in mg/l. EC: Electric conductivity, TDS: Total dissolved solids (mg/l)

[a] EDR-1 is from taken Yalçın (2007), ED-3[b] and EDJ-2[b] are taken from Avşar et al. (2013), IGJ-2[c] is taken from Kaçar et al. (2017).

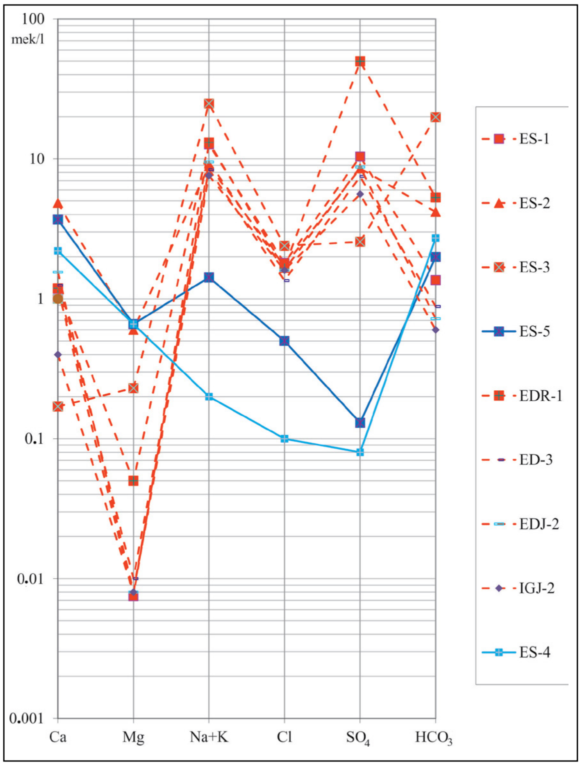

Figure 12- Semi-logarithmic Schoeller diagram for thermal (red dashed lines) and cold (blue lines) waters in Edremit and Güre areas. (Sample numbers refer to sample site numbers in Table 2 and Figure 5).

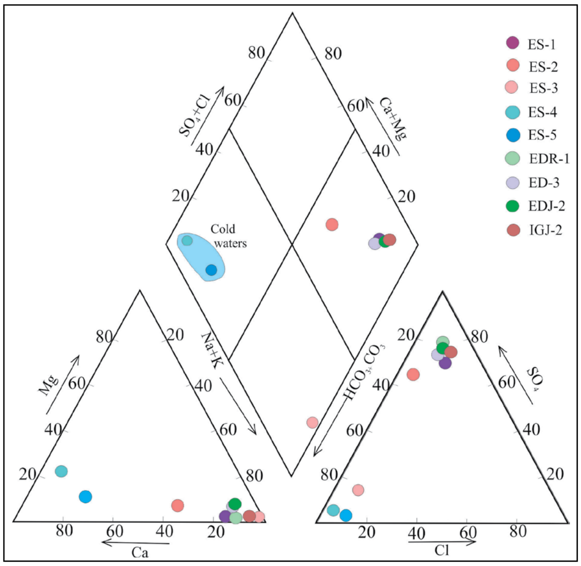

Figure 13- Piper diagram for thermal and cold waters in Edremit and Güre (Sample numbers refer to sample site numbers in Table 2 and Figure 5).

Table 7- Results for stable isotope (‰), tritium and Cl- for the Edremit-Güre waters.

Sample No	Temperature °C	Date of sampling	$\delta^{18}O$ (VSMOW)	δD (VSMOW)	Deuterium excess	^{3}H (TU)	Cl^- (mg/l)
ES-1	86	5.11.2019	-7.72	-47.04	14.7	0.46	64.9
ES-2	32	5.11.2019	-7.37	-43.71	15.3	5.84	61.3
ES-3	32	6.11.2019	-7.32	-43.91	14.7	1.11	82.1
ES-4	15	7.11.2019	-7.76	-41.64	20.4	2.97	3.6
ES-5	19	7.11.2019	-7.19	-41.71	15.8	1.4	20.7
EDR-1^{a}	60	-	-7.26	-47.25	10.8	0	59
ED-3^{b}	62	10.09.2008	-9.19	-52.19	21.3	-*	48

^{a}: EDR-1 is from taken Yalçın (2007), ^{b}: ED-3 is from taken Avşar et al. (2013), *: This information is not available in the reference in question.

4.3.2. Isotope Geochemistry

The results of isotope analysis of water samples are given in Table 7. The values are presented in per mil (‰) deviations from the Vienna SMOW standard. In the $\delta^{18}O$–$\delta^{2}H$ graphic, isotope compositions of Edremit-Güre waters are plotted between the Marmara Meteoric Water Line (MMWL) ($\delta^{2}H=8\delta^{18}O+15$; Eisenlohr, 1995) and the Global Meteoric Water Line (GMWL) ($\delta^{2}H = 8\delta^{18}O + 10$; Craig, 1961). The $\delta^{18}O$ of thermal springs varies from –7.72 to –6.48‰ and from –7.76 to –5.87‰ for the cold waters. The δD values are in the range of –47.04 to –38.3‰7 for thermal waters and between –41.71 and –32.16‰ for cold waters (Figure 14). In general, $\delta^{18}O$–δD values of thermal waters are slightly lower than cold waters.

Much negative isotope values of thermal waters (enriched in light isotopes) indicate that they are recharged from higher altitudes than the cold waters (Figure 14). Accordingly, the waters might have negative isotope values on the Marmara meteoric water line and are not involved in a deep circulation, and cold surface waters may have mixed with these waters.

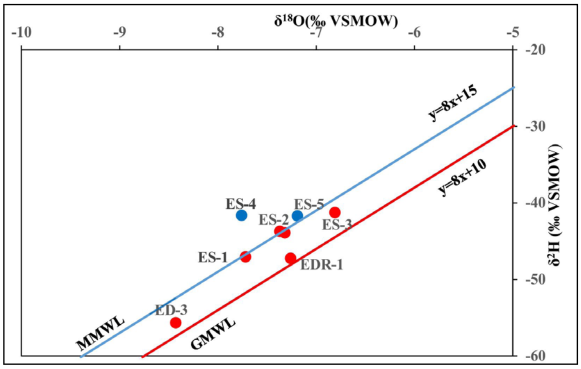

Figure 14- $\delta^{18}O$ and $\delta^{2}H$ diagram of the water samples. [MMWL: Marmara Meteoric Water Line (Eisenlohr, 1995); GMWL: Global Meteoric Water Line (Craig, 1961)]. Thermal waters are represented by red circles, while cold waters are represented by blue circles.

The deuterium excess of the samples calculated with the formula of d= δD-8*$\delta^{18}O$ varies between 14.7 and 21.3‰. The high values of deuterium excess indicate that waters in this region are recharged by marine precipitation. The sample ES-4 with the highest deuterium excess value is enriched in heavy isotope with respect to other samples and at the same time, it could be recharged from higher elevations and does not show any evaporation effect.

Tritium is an excellent tracer for water circulation. It is used for determining the relative age of groundwaters since it is radioactive (with half-life of 12.43 years) (Clark and Fritz, 1997). The concentration of tritium in meteoric waters is given in Tritium Unit (TU) (1 TU=1 atom $^{3}H/10^{18}$ atom H). The concentration of tritium in the atmosphere has changed by the nuclear tests. Atmospheric tritium concentration before 1963 was around 5 TU and it reached a maximum about 3000 TU in 1963 with tritium emitted into the atmosphere by nuclear tests (Mazor, 1991). According to these data, samples ES-1 and EDR-1 might be recharged by precipitation before 1963. The EDR sample has ^{3}H content of 0 TU, indicating a relatively deep circulation and a long residence time.

Tritium-Cl graph is very useful to examine the circulation depth of waters (Akıllı and Mutlu, 2018) (Figure 15). The low tritium value indicates that the waters are deeply circulated and have longer residence time underground. In addition, the tritium values of deep circulating waters are quite low and their chloride content is high. Chloride is a widely used ion in the exploration and interpretation of geothermal systems. It directly characterizes geothermal water as it is not easily absorbed by other minerals once dissolved. This shows that thermal waters have longer residence time and their chemical composition is much more modified by the water-rock interaction (increasing chloride content). It is likely that sample ES-3 has a deeper circulation than other thermal water samples. The fact that the tritium content of the cold waters samples is higher than the geothermal waters (except for sample ES-2) indicates that these waters have a shallow circulation. The sample ES-2 was taken from a shallow well (64 m) drilled in alluvium. In terms of high tritiumm value and low chloride content, this sample suggests that there is a mixture of cold water with thermal water. The temperature of ES-2 sample is 32ºC. As seen in the Piper diagram (Figure 13), the ES-2 sample falls into a separate zone from other thermal waters. The high tritium and low chloride values of this sample might indicate a mixing with cold groundwater (Figure 15).

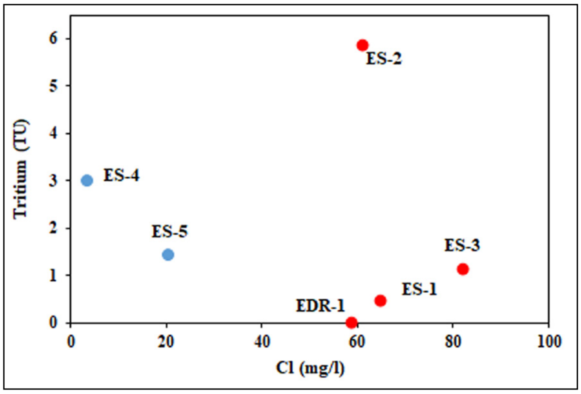

Figure 15- Tritium versus chloride diagram of water samples. Thermal waters are represented by red circles, while cold waters are represented by blue circles.

The relation between oxygen-18 and tritium is correlated with recharge elevation of the waters and their residence time in the aquifer. The residence time of waters increases as it approaches to the origin along the vertical axis of the graph. As seen in Figure 16, thermal water samples with low tritium value have a long residence time underground circulation, while cold waters with high tritium content have a shorter circulation. The sample ES -5 has a deeper circulation than ES-4 which is recharged from precipitation falling at higher elevations.

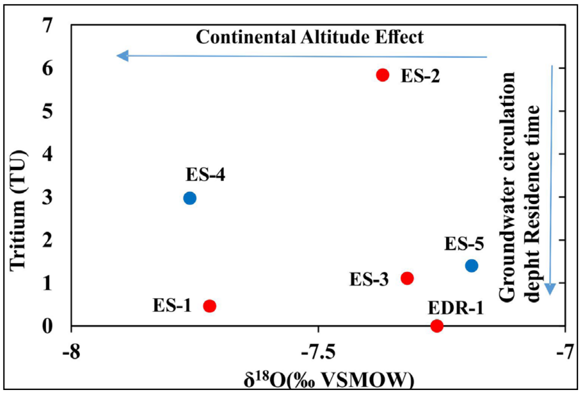

Figure 16- Plot of ^{3}H - δ^{18}O diagram of the water samples. Thermal waters are represented by red circles, while cold waters are represented by blue circles.

4.3.3. Geothermometer Applications

To determine the reservoir temperatures of the Edremit-Güre thermal waters, various geothermometers and mineral equilibrium models were used. First, we considered the maturity index (MI) to decide the applicability of Na-K geothermometers to the samples. The maturation index of the thermal waters, except for ES-2 sample, is found >2 and therefore, both cation and silica geothermometers were calculated (Figure 17). For samples with a maturation index less than 2, the application of cation geothermometers may yield erroneous results and therefore, silica geothermometers were preferred, which are based on mineral solubility and give better results at low temperatures (Akıllı and Mutlu, 2018) (Table 8). In Figure 17, sample ES-2 is close to the

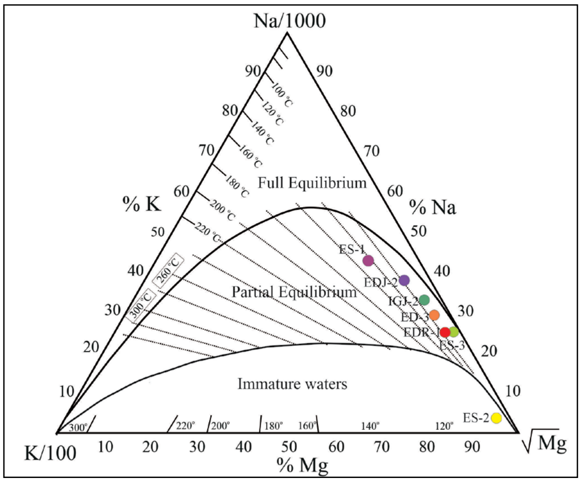

Figure 17- Na-K-Mg equilibrium diagram of Giggenbach (1988).

Table 8- Geothermometer estimates for Edremit thermal waters.

Sample No	**T (ºC)**	**Quartz** (Fournier and Potter, 1982)	**Quartz** (no steam loss) (Fournier, 1973)	**Chalcedony** (no steam loss, Fournier, 1977)	**Chalcedony** (no steam loss, Arnorsson et al., 1983)	**K-Mg** (Giggenbach, 1988)	**Na-K** (Fournier, 1979)	**Na-K** (Giggenbach et al., 1983)
ES-1	86	124	124	96	95	89	126	146
ES-2	32	84	83	52	55	-	-	-
ES-3	32	83	82	51	53	64	61	83
EDR-1	60	109	109	79	80	77	104	125
ED-3	62	83	82	51	53	65	97	117
EDJ-2	58	102	102	72	73	77	117	137

Mg corner and plots into the “immature waters” field. Only quartz and chalcedony geothermometers were applied to this sample. Other thermal water samples are plotted in the “partially equilibrated waters” field. For these waters, both cation and silica geothermometers were applied.

The temperatures of 82 and 124ºC were calculated by quartz (no steam loss) geothermometers of Fournier (1973) and Fournier and Potter (1982) (Table 8). For the chalcedony geothermometer, the equations of Fournier (1977) and Arnorsson et al (1983) were used. The reservoir temperatures of waters estimated by these geothermometers are 51-96ºC and 53-95ºC, respectively, which yielded very close values. The cation geothermometers are based on the distribution of alkaline elements between solid and liquid phases. The cation geothermometers are suitable for high-temperature waters where reservoir temperatures are > 180 ºC and may give incorrect results for low- temperature waters. The reservoir temperatures estimated with cation geothermometers vary between 61 and 137 ºC (Table 8). The cation geothermometers yielded different reservoir temperature values due to the interaction of the water with the host rocks and the mixing with cold water during the rise to the surface. Considering that silica saturation is controlled by chalcedony rather than quartz at temperatures below 180ºC (Fournier, 1991), the reservoir temperatures calculated by the chalcedony geothermometer are thought to be more realistic (Akıllı and Mutlu, 2018).

4.4. GIS Application

The geological features of the basin were investigated by applying five groups of studies. These are; 1) 1/100.000-1/25.000 scaled geological maps from the MTA archives, 2) lithological units in the basin with 1/100.000 scaled geological maps and literature data (MTA reports, articles, etc.), 3) stratigraphic succession of the basin, 4) determination of rocks that can be heaters and reservoirs in a geothermal system on the stratigraphic column section and 5) all these data is used to construct a conceptual model of the basin using the GIS analyses combined with thermal and alteration remote sensing results (Figure 18). The outputs are displayed on the SRTM-relief map for a final evaluation. Tectonic structures, kinematic analyses, geological units and stratigraphic sequence of the study area are the key components for such studies. Within the scope of hydrogeological studies, the samples collected from the thermal and cold waters in the area were evaluated using water chemistry, isotope analysis and various diagrams. As a result of these studies, data on chemical compositions of waters, circulation depths of thermal waters (shallow or deep), reservoir temperatures, types of reservoir rocks and recharge elevations were obtained. This information forms the hydrogeological spatial data layers in the study. The above-mentioned spatial data layers are composed of four main groups that are remote sensing, tectonics, geological and hydrogeological studies.

For the remote sensing studies, three groups of spatial data were produced. The first is the daytime average and the ASTER nighttime LST maps. The daytime average LST map was prepared taking the arithmetic average of the maximum 10ºC temperature values of the ASTER daytime, Landsat 8 TIRS and Lansdat 7 ETM+ maps to increase the accuracy. The second data layer is the band ratio analysis results of ASTER Level 1T satellite images to determine the hydrothermal alteration zones and minerals associated with geothermal systems. The SBAS analysis of ALOS Palsar-1 SAR images within the scope of remote sensing studies, the LOS displacement map of

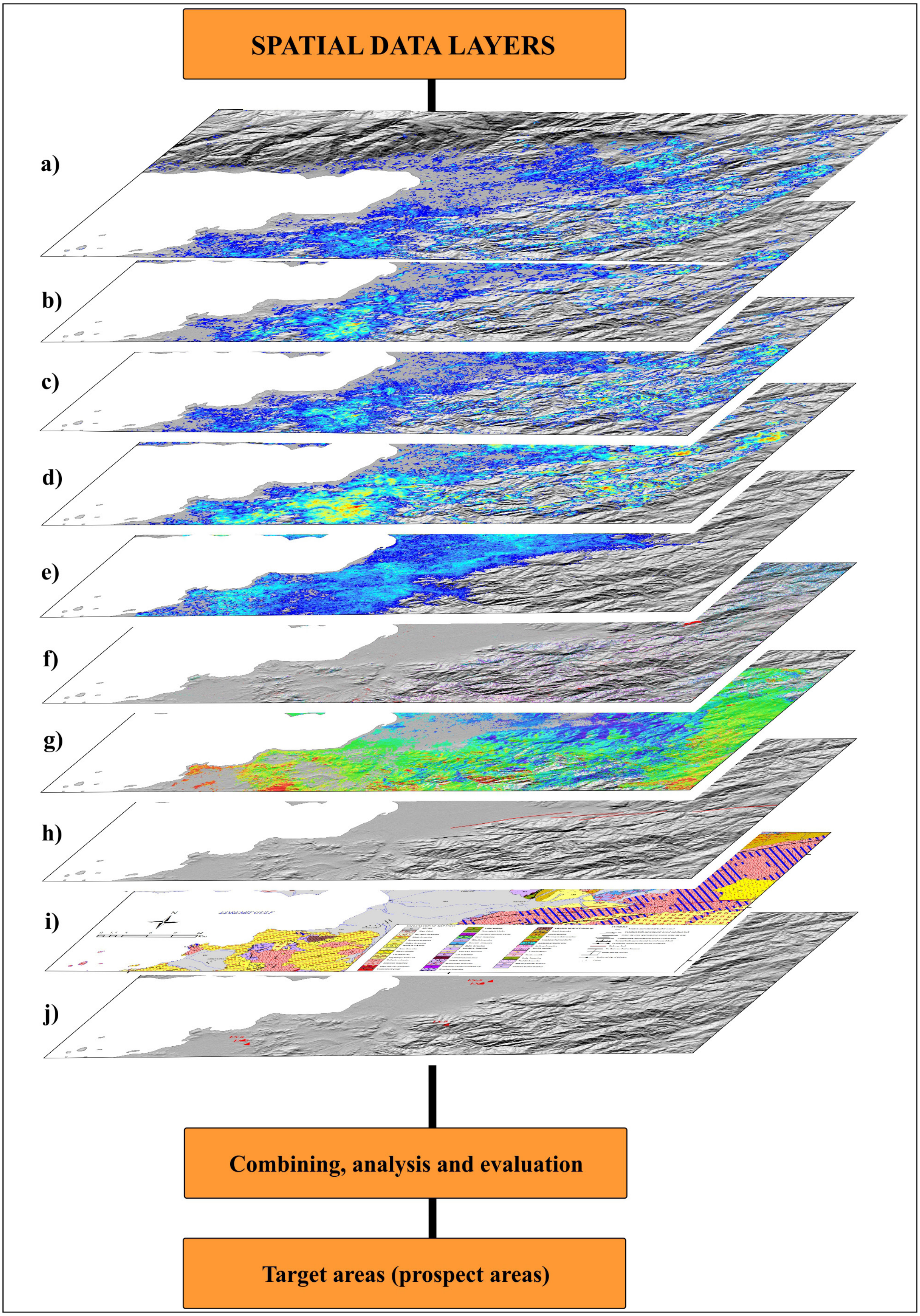

Figure 18- Spatial data layers and flow chart of GIS studies: a) ASTER-daytime LST, b) Landsat 8 TIRS LST, c) Landsat 7 ETM+ LST, d) Daytime-average LST, e) ASTER-nighttime LST, f) Hydrothermal alteration, g) ALOS Palsar-1 SBAS-deformation, h) Tectonic framework and kinematic analysis, i) Geology, j) Hydrogeology.

the surface deformations (subsidence, uplift, etc.) was prepared. All these results represent the combinations and assessment of the layers using the geographical information system (GIS), which is recently widely used in many disciplines for viewing, combining, organizing, querying, analyzing, and evaluating, spatial data layers (Bonham-Carter, 1994; Carranza, 2009). Finally, their combination, provides an, opportunity to define probable target areas (prospect areas) that might be important in terms of geothermal energy (Figure 19).

5. Discussion

During a geothermal energy exploration and evaluation study, several stages are progressed from initial exploration to production (Van der Meer et al., 2014). In this research, we carried out a pilot study in the Edremit Basin, Balıkesir, to evaluate the geothermal potential and to determine possible target areas with the use of a number of data, which include structural controls, hydrogeological features, and satellite image analyses.

Ten different layers were used to describe the possible target fields in the basin (Figure 19). Determining potential target areas (prospects) in terms of geothermal energy might provide significant gains in cost, labor and time. For this reason, we compared our results to known geothermal resources. Additionally, a fieldwork was carried out to check the reliability of thermal anomalies. For example, solar panels or man-made structures such as factory reflect huge thermal anomalies and mislead the data.

Surface temperature values calculated from ASTER-nighttime/daytime, Landsat 8 TIRS and Landsat 7 ETM+ thermal bands were validated using geothermal resources known in the region. Sample ES-3 located at northeast of Armutova has a temperature of 33ºC and reservoir temperature of this sample estimated by chalcedony geothermometer of is 53 ºC. In the average daytime LST map (without reclassification), the highest temperature was estimated 37 ºC. In this map, temperature values around the thermal springs are found in about the range of 30 to 32 ºC. In the average daytime LST map, that was obtained using highest temperature value of nearly 10 ºC and reclassification, we obtained temperatures of 4-5 ºC (the highest relative value is 12 ºC). Samples ED-3, ES-2 and EDJ-2 that are associated with E-W trending fault at the south of Edremit have temperatures of 62, 32 and 58 ºC, respectively. Reservoir temperatures of these samples estimated by chalcedony geothermometer are 53, 55 and 73ºC. In the average daytime LST map (without reclassification), temperature around the samples are estimated approximately 29-32ºC. In the average daytime reclassified LST map, temperatures values of about 4-7 ºC were obtained. ES-1 and EDR-1 samples associated with E-W trending active fault at the south of Güre have temperatures of 86 and 60ºC. Chalcedony reservoir temperatures of these samples are 95 and 80ºC. In the average daytime LST map (without reclassification) temperatures are estimated 28-30 ºC around these samples and in the average daytime reclassified LST map, temperatures are relatively found approximately 4-5 ºC.

Each of the areas that were selected for confirmation are represented by higher LST values with respect to surrounding parts. It is noticeable that high LST values are consistent with faults and fault systems that trend in E-W direction parallel to the main strike of NAFZ. The use of thermal satellite images for the correct identification of geothermal anomalies requires the integration of geological and tectonic data. The combination of all data considerably increases the determination of reliable information. According to the findings of the kinematic analysis, the expansion direction of the basin is in the N-S direction. As a result, E-W trending faults and their surrounding areas can be considered as potential areas for geothermal exploration and evaluation studies in the basin.

It is critical for the success of geothermal energy exploration studies to identify hydrothermal alteration minerals and/or mineral groups as surface indicators of geothermal activity. According to the results of the band ratio analysis of the ASTER images, in around geothermal springs in the west of the Güre, extensive argillization, silicification, and alunite/kaolinite anomaly areas were observed on granodiorite porphyry (PgoNkp) and Oligo-Miocene granodiorites (PgoNg), which are considered to be reservoir rocks (Figure 20). In the north of Edremit, Oligo-Miocene granodiorite (PgoNg) has been exposed to widespread hydrothermal alteration. ASTER band ratio analysis revealed argillization, silicification, and alunite/kaolinite anomaly areas on this unit.

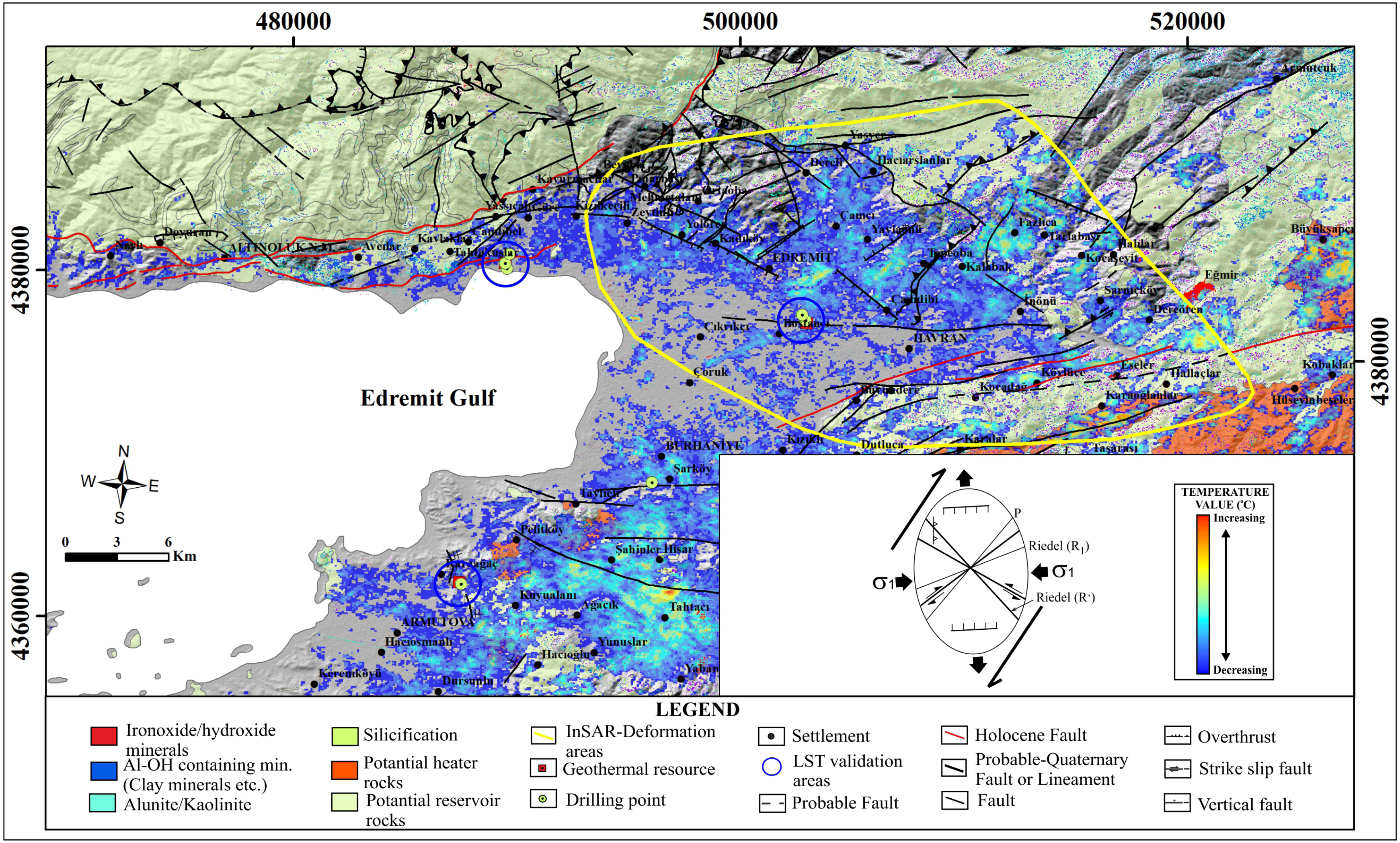

Figure 19- Final output map of the study area. Blue circles indicate the high possibility areas and recent geothermal resources (Faults and active faults: Duru et al., 2004; Duru et al., 2007*a, b*; Dönmez, 2013; Emre et al., 2011; faults determined during the field study).

Figure 20- A view from the hydrothermally altered Granodiorite porphyry units in east of Havran.

In the Oligo-Miocene granodiorite (PgoNg) to the north of Edremit, extensive argillization, silicification, and alunite/kaolinite anomaly areas emerged. In addition, widespread argillization, silicification, and alunite-kaolinite anomaly areas were observed on the Yurekli Dacite (Nmy) and Bozdivlit volcanite (Nmb) which are considered as the heat source of geothermal resources in the northeast and southeast part of Armutova. In the field studies, samples were collected from these alteration areas. The alunite, illite, and montmorillonite minerals were identified in the spectral analysis of the samples (Figure 21). Ironoxide and hydroxide minerals are highly prevalent that can be related to hydrothermal and surface meteoric waters. As a result, all ironoxide and hydroxide mineral anomalies observed in ASTER image analysis should not be considered to be of a hydrothermal origin.

In the area between the faults bordering the south and north of the Edremit basin, subsidence has appeared as a distinctive feature of the ALOS Palsar-1 SBAS analysis results. This area is situated on the downward block of faults that border the north and south parts of the basin. Surface deformations observed in ALOS Palsar-1 SBAS analyses could have been caused by human activity, lithological features, or erosion in some areas. The subsidence event detected in the basin by the ALOS Palsar-1 SBAS analysis can be interpreted as an indicator of crustal thinning in pull-apart basins. Crustal thinning may contribute more to heat transport and conduction through tectonic structures in pull-apart basins than in other regions.

In the early stages of geothermal exploration and evaluation studies, satellite data analysis such as LST, the determination of hydrothermal alteration anomaly areas and mienrals is effective and useful approach to determine target prospect areas. The results of the studies have demonstrated that, in order to determine the prospect areas in pull-apart basins with greater accuracy and success, the LST results, in particular, should be evaluated considering the compression-extension directions in the basin.

6. Conclusions

Remote sensing, geological, tectonic, and hydrogeological research was carried out in the Edremit (Balıkesir) Basin in order to reveal geothermal energy potential and identify prospect areas for detailed surveys (drilling, geophysics, gas measurements, detail mapping, etc.). The findings of these studies were evaluated using GIS tools.

High temperature values were obtained in the LST maps around known geothermal resources in the basin, and they were found to be compatible. When the results of the study are evaluated considering the tectonic

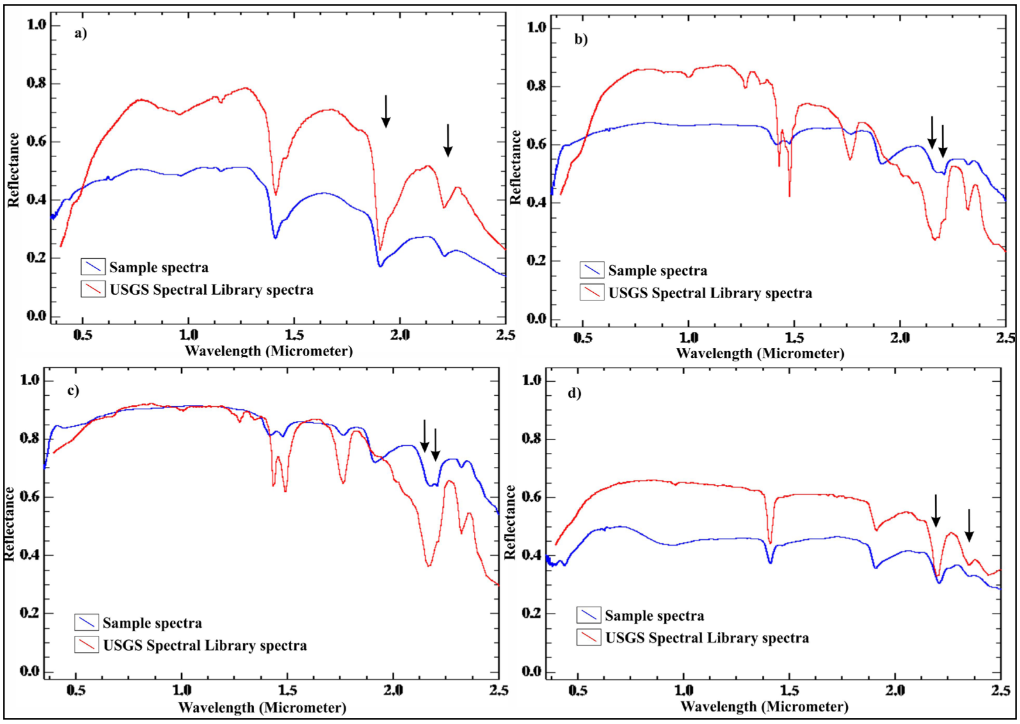

Figure 21- Spectra of hydrothermal alteration samples collected from east of Havran and mineral spectra in the USGS Spectral Library (USGS, 2007): a) Montmorillonite (sample no 1), b) and c) Alunite (sample no 2), c) illite (example no. 3) (sample locations are given in Figure 10)

structures and the compression-extension aspects of the basin, it is seen that the basin has a potential in terms of geothermal energy exploration. It is seen that there are many prospect areas that can be favorable for detailed studies within the basin. The applied approach and method were found to be effective based on the validation results of LST values computed from the daytime and nighttime thermal bands (ASTER-daytime, Landsat 8 TIRS, Landsat 7 ETM+ and ASTER-nighttime). The study also demonstrated that satellite data analyses (LST, hydrothermal alteration, MT-InSAR, etc.) achieve accurate, successful, and efficient results for identifying prospect areas in the preliminary phase of geothermal exploration and evaluation studies.

Acknowledgement

This study was financially supported by the General Directorate of Mineral Research and Exploration. The authors are grateful to anonymous referees for their critical comments that improved the manuscript. Project name is “Kuzey Anadolu Fay Sistemi Ve Doğu Anadolu Fay Sistemi Boyunca Gelişmiş Havzaların Jeotermal Enerji Potansiyellerinin Uzaktan Algılama ve Coğrafi Bilgi Sistemleri (CBS) Yöntemleri ile İncelenmesi: 3- Edremit (Balıkesir) Havzası”.

References

Akıllı, H., Mutlu, H. 2018. Polatlı ve Haymana (Ankara) sıcak sularının kökenine yönelik kimyasal ve izotopik sınırlamalar. Yerbilimleri 39 (1), 41-64.

Aktuğ, B., Nocquet, J. M., Cingoez, A., Parsons, B., Erkan, Y., England, P., Lenk, O., Guerdal, M.A., Kılıçoğlu, A., Akdeniz, H., Tekgüzel, A. 2009. Deformation of western Turkey from a combination of permanent and campaign GPS data: Limits to block-like behavior. Journal of Geophysical Research-Solid Earth, 114, B10404, doi:10.1029/2008JB006000.

Allis, R.G., Nash, G.D., Johnson, S.D. 1999. Conversion of thermal infrared surveys to heat flow: comparisons from Dixie Valley, Nevada, and Wairakei, NewZealand. Geothermal Resources Council – Transactions 23, 499–504.

Altunkaynak, Ş., Genç, S. 2008. Petrogenesis and time-progressive evolution of the Cenozoic continental volcanism in the Biga Peninsula, NW Anatolia (Turkey). Lithos 102, 316–340.

Angelier, J. 1979. Determination of the mean principal directions of stresses for a given fault population. Tectonophysics 56, T17-T26.

Angelier, J. 1984. Tectonic analysis of fault slip data sets. Journal of Geophysical Research 89, 5835-5848.

Arnorsson, S., Gunnlaugsson, E., Svavarsson, H. 1983. The Chemistry of Geothermal Waters in Iceland III, Chemical Geothermometry in Geothermal Investigations. Geochimica et Cosmochimica Acta 47, 567-577.

Artis, D.A., Carnahan, W.H. 1982. Survey of emissivity variability in thermography of urban areas. Remote Sensing of Environment 12(4), 313–329.

Avşar, Ö. 2011. Geochemical Evaluation and Conceptual Modeling of Edremit Geothermal Field. A Thesis Submitted to the Graduate School of Natural and Applied Sciences of Middle East Technical University, Ankara.

Avşar, Ö., Güleç, N., Parlaktuna, M. 2013. Hydrogeochemical characterization and conceptual modeling of the Edremit geothermal field (NW Turkey). Journal of Volcanology and Geothermal Research 262, 68-79.

Ayenew, T. 2001. Surface kinetic temperature mapping using satellite spectral data in Central Main Ethiopian Rift and adjacent highlands. Ethiopian Journal of Science 24, 51–68.

Aygül, M., Topuz, G., Okay, İ. A., Satır, M., Meyer, H.P. 2012. The kemer metamorphic complex (NW Turkey): A subducted continental margin of the Sakarya Zone. Turkish Journal of Earth Sciences 21, 19–35.

Barsi, J.A., Barker, J.L., Schott, J.R. 2003. An Atmospheric Correction Parameter Calculator for a Single Thermal Band Earth-Sensing Instrument. IGARSS03, 21-25 July 2003, Centre de Congres Pierre Baudis, Toulouse, France.

Barsi, J.A., Schott, J.R., Palluconi, F.D., Hook, S.J. 2005. Tool for Single Thermal Band Instruments. Earth Observing Systems X, Proc. SPIE 5882, August 2005, San Diego, CA.

Beccaletto, L. 2003. Geology, correlations, and geodynamic evolution of the Biga Peninsula (NW Turkey). Géologie appliquée. Université de Lausanne, Français.

Berardino, P., Fornaro, G., Lanari, R., Sansosti, E. 2002. A new algorithm for surface deformation monitoring based on small baseline differential SAR interferograms. IEEE Transactions on Geoscience and Remote Sensing 40/11, 2375–2383.

Bingöl, E. 1969. Kazdağ Masifinin merkezi ve Güneydoğu kesiminin jeolojisi. Bulletin of the Mineral Research and Exploration 72, 110-123.

Bingöl, E. 1971. Fiziksel yaş tayini metodlarını sınıflama denemesi ve Rb-Sr ve K-Ar metodlarının Kazdağ'da bir uygulaması. Türkiye Jeoloji Kurumu Bülteni 14, 1-16.

Bingöl, E., Delaloye, M., Ataman, G. 1982. Granitic intrusion in Western Anatolia; a contribution to the geodynamic study of this area. Eclo- Geol. Helv. 75/2, 437-446.

Bingöl, E., Delaloye, M., Pişkin, A., Genç, Ş. 1992. Significance of the granitoids of Eastern and Southern Marmara within the framework of the regional geotectonic evolution: Abstract of the Şnterna. Symp. Geol. Black Sea Region, Maden Tetkik ve Arama Genel Müdürlüğü.

Bonham-Carter, G.F. 1994. Geographic Information Systems for Geoscientists: Modelling with GIS. Pergamon: Elsevier Science Ltd Press.

Bozkurt, E., Mittwede, S.K. 2001. Introduction to the geology of Turkey - a synthesis. International Geology Review 43, 578–594.

Boztepe Güney, A., Yılmaz, Y., Demirbağ, E., Ecevitoğlu, B., Arzuman, S., Kuşçu, I. 2001. Reflection seismic study across the continental shelf of Baba Burnu promontory of Biga Peninsula, northwest Turkey. Marine Geology 176(1–4), 75–85.

Braddock, M., Biggs, J., Watson, I. M., Hutchison, W., Pyle, D. M., Mather, T. A. 2017. Satellite observations of fumarole activity at Aluto volcano, Ethiopia: Implications for geothermal monitoring and volcanic hazard. Journal of Volcanology and Geothermal Research 341, 10.1016/j.jvolgeores.2017.05.006.

Bulut, M., Purtul, E., Destur, M., Yılmaz, B.E. 2018. Karaağaç (Gömeç-Balıkesir) Ar:10/0003 Nolu Jeotermal Kaynak Arama Ruhsat Sahası Jeotermal Etüt (Jeoloji-Jeofizik) ve BGK-2011/9 jeotermal Araştırma Sondajı Kuyu Bitirme Raporu. General Directorate Mineral Research and Exploration Report No: 13716, Ankara (unpublished).

Calderon-Chaparro, R., Vargas-Cuervo, G. 2019. Determination of Hydrothermal Prospects in Paipa Geothermal Region (Boyacá, Colombia) Using Remote Sensing and Field Data. Earth Sciences Research Journal 23, 265-282. 10.15446/esrj.v23n4.77810.

Calvin, W.M., Littlefield, E.F., Kratt, C. 2015. Remote sensing of geothermal-related minerals for resource exploration in Nevada. Geothermics 53, 517-526.

Calvin, W., Pace, E. 2016. Mapping alteration in geothermal drill core using a field portable spectroradiometer. Geothermics 61. 10.1016/j.geothermics.2016.01.005.

Carranza, E.J.M. 2009. Geochemical anomaly and mineral prospectivity mapping in GIS, Handbook of Exploration and Environmental Geochemistry. Amsterdam: Elsevier 11, 351.

Chan, H.P., Chang, C. P. 2018. Exploring and monitoring geothermal and volcanic activity using Satellite Thermal Infrared data in TVG, Taiwan. Terrestrial, Atmospheric and Oceanic Sciences 29, 387-404. 10.3319/TAO.2018.01.22.01.

Chan, H. P., Chang, C. P., Dao, P. 2018. Geothermal Anomaly Mapping Using Landsat ETM+ Data in Ilan Plain, Northeastern Taiwan. Pure and Applied Geophysics 175. 10.1007/s00024-017-1690-z.

Clark, I., Fritz, P. 1997. Environmental isotopes in hydrogeology. Lewis Publishers, New York, 328.

Craig, H. 1961. Isotopic variations in meteoric waters. Science 133, 1833-1834.

Didik, S., Ölmez, E., Güner, A., Yıldırım, N. 1994. Balıkesir Edremit Güre G1 ve G2 Sıcak Su Sondajları Kuyu Bitirme Raporu. Maden Tetkik ve Arama Genel Müdürlüğü, Rapor No: 9837, Ankara (unpublished).

Dilemre, A., Gökalp, Y., Hakyol, S., Sarp, S., Orakçı, A. 2006. Balıkesir İli Jeotermal Kaynakları Değerlendirme Raporu. Maden Tetkik ve Arama Genel Müdürlüğü, Rapor No: 10858, Ankara (unpublished).

Dönmez. M. 2013. 1:100.000 Ölçekli Türkiye Jeoloji Haritaları, No:193 Ayvalık-J17 Paftası. Maden Tetkik ve Arama Genel Müdürlüğü, Ankara.

Dönmez, M., Akçay, A.E., Genç, Ş.C., Acar, Ş. 2005. Biga Yarımadası'nda Orta-Üst Eosen volkanizması ve denizel ignimbiritler. Bulletin of the Mineral Research and Exploration 131, 49-61.

Duru, M., Pehlivan, Ş., Şentürk, Y., Yavaş, F., Kar, H. 2004. New results on the lithostratigrapy of the Kazdağ Massif in nortwest Turkey. Turkish Journal of Earth Sciences "A special issue commemorating, Okan Tekeli", 177-186.

Duru, M., Pehlivan, Ş., Ilgar, A., Dönmez, M., Akçay, A.E. 2007*a*. 1:100.000 Ölçekli Türkiye Jeoloji Haritaları, No:98 Ayvalık-İ17 Paftası. Maden Tetkik ve Arama Genel Müdürlüğü, Ankara.

Duru, M., Pehlivan, Ş., Ilgar, A., Dönmez, M., Akçay, A.E. 2007*b*. 1:100.000 Ölçekli Türkiye Jeoloji Haritaları, No:97 Balıkesir-İ18 Paftası. Maden Tetkik ve Arama Genel Müdürlüğü, Ankara.

Eisenlohr, T. 1995. Die Thermalwässer der Armutlu-Halbinsel (NW Türkei) und deren Beziehung zu Geologie und aktiver Tektonik. Dissertation, ETH Zurich No: 11340, 165.

Emre, Ö., Duman, T. Y., Özalp, S. 2011. 1:250.000 Ölçekli Türkiye Diri Fay Haritası Serisi, Ayvalık (NJ 35-2) Paftası, Seri No:2, Balıkesir (NJ 35-3) Paftası, Seri No:4, Maden Tetkik ve Arama Genel Müdürlüğü, Ankara-Türkiye.

Erzenoğlu, Z., 1985. Balıkesir Edremit Güre (Demet)-1 sıcaksu sondajı kuyu bitirme raporu. Maden Tetkik ve Arama Genel Müdürlüğü Report, No. 7881 (in Turkish), Ankara (unpublished).

Faulds, J.E., Coolbaugh, M.F., Vice, G.S., Edwards, M.L. 2006. Characterizing Structural Controls of Geothermal Fields in the Northwestern Great Basin: A Progress Report. Geothermal Resources Council Transactions 30, 69–76.

Fournier, R.O. 1973. Silica in Thermal Waters: Laboratory and Field Investigations. Proceedings of the International Symposium on Hydrogeochemsitry and Biochemistry, Tokyo, Vol.1, Clark Co., Washington D.C. 122-139.

Fournier, R.O. 1977. Chemical Geothermometers and Mixing Models for Geothermal Systems. Geothermics 5, 41-50.

Fournier, R.O. 1979. A Revised Equation for the Na/K Geothermometer, Geoth. Res. Council. Transactions 3, 221-224.

Fournier, R.O. 1991. Water geothermometers applied to geothermal energy. In: D'Amore, F. (coordinator), Application of Geochemistry in Geothermal Reservoir Development. UNITAR/UNDP publication, Rome, 37-69.

Fournier, R.O., Potter, R.W. 1982. A Revised and Expanded Silica (Quartz) Geothermometer. Geoth. Res. Council Bull. 11-10, 3-12.

Genç, Ş.C., Dönmez, M., Akçay, A.E., Altunkaynak, Ş., Eyüpoğlu, M., Ilgar, Y. 2012. Biga Yarımadası

Tersiyer volkanizmasının stratigrafik, petrografik ve kimyasal özellikleri. In: Yüzer, E., Tunay, G. (Eds.), Biga Yarımadasının Genel ve Ekonomik Jeolojisi. Bulletin of the Mineral Research and Exploration 28, 122–162.

Gessner, K., Gallardo, L. A., Markwitz, V., Ring, U., Thomson, S. N. 2013. What caused the denudation of the Menderes Massif: Review of crustal evolution, lithosphere structure, and dynamic topography in southwest Turkey. Gondwana Research 24(1), 243-274.

Gillespie, A. R., Rokugawa, S., Matsunaga, T., Cothern, J. S, Hook, S., Kahle, A. B. 1998. A Temperature and Emissivity Separation algorithm for Advanced Spaceborne Thermal Emission and Reflection radiometer ASTER images. IEEE Transactions on Geoscience and Remote Sensing 36, 1113–1126.

Giggenbach, W.F. 1988. Geothermal Solute Equilibria, Derivation of Na-K-Mg-Ca Geoindicators, Geochim. Cosmochim. Acta 52, 2749-2765.

Giggenbach, W.F., Gonfiantini, R., Jangi, B.L., Truesdell, A.H. 1983. Isotopic and Chemical Composition of Parbatia Valley Geothermal Discharges, NWHimalaya, India. Geothermics 12, 199-222.

Giordano, G., Pinton, A., Cianfarra, P., Baez, W., Chiodi, A., Viramonte, J., Norini, G., Groppelli, G. 2013. Structural control on geothermal circulation in the Cerro Tuzgle-Tocomar geothermal volcanic area (Puna Plateau, Argentina). Journal of Volcanology and Geothermal Research 249, 77–94.

Gutierrez, F., Lemus, M., Parada, M., Benavente, O., Aguilera, F. 2012. Contribution of ground surface altitude difference to thermal anomaly detection using satellite images: Application to volcanic/geothermal complexes in the Andes of Central Chile. Journal of Volcanology and Geothermal Research 237-238, 69-80.

Güner, A., Didik, S., Ölmez, E., Yıldırım, N. 1994. Balıkesir-Edremit-Güre (G-1 ve G-2) sondajları kuyu bitirme raporu. Maden Tetkik ve Arama Genel Müdürlüğü Derleme Rapor No: 9837, 16, Ankara (unpublished).

Gürer, Ö. F., Sangu, E., Özburan, M., Gürbüz, A., Gürer, A., Sinir, H. 2016. Plio-Quaternary kinematic development and paleostress pattern of the Edremit Basin, western Turkey. Tectonophysics 679, 199–210.

Gürer, Ö. F. 2023. A new look at the origin of N-S trending young basins of western Anatolia. Bulletin of the Mineral Research and Exploration 170, 117-146.

Haselwimmer, C.E., Prakash, A. 2013. Thermal Infrared Remote Sensing of Geothermal Systems. In: Kuenzer, C., Dech, S. (Eds.), Thermal Remote Sensing: Sensors, Methods, and Applications 453–473.

Hewson, R.D., Cudahy, T.J., Mizuhiko, S., Ueda, K. and Mauger, A.J., 2005. Seamless geological map generation using ASTER in the Broken Hill-Curnamona province of Australia. Remote Sensing of Environment, 99, 159-172.

Hewson, R., Robson, D., Carlton, A., Gilmore, P. 2017. Geological application of ASTER remote sensing within sparsely outcropping terrain, Central New South Wales, Australia. Cogent Geoscience 3, 10.1080/23312041.2017.1319259.

Hook, S., Abbott, E., Grove, C., Kahle, A., Palluconi, F. 1999. Multispectral thermal infrared data in geological studies. In: Rencz, A.N., Ryerson, R.A. (Eds.), Manual of Remote Sensing, 3rd Ed. Remote Sensing for the Earth Sciences 3. Wiley 59–110.

Hulley, G., Hughes, C., Hook, S. 2012. Quantifying uncertainties in land surface temperature and emissivity retrievals from ASTER and MODIS thermal infrared data. Journal of Geophysical Research (Atmospheres), 117, 23113. 10.1029/2012JD018506

Ilgar, A., Demirci-Sezen, E., Demirci, Ö. 2012. Biga Yarımadası Tersiyer İstifinin Stratigrafisi ve sedimantolojisi. In: Yüzer, E., Tunay, G. (Eds.), Biga Yarımadasının Genel ve Ekonomik Jeolojisi. MTA Özel Yayın Serisi-28, 75-120.

Jackson, J., McKenzie, D.P. 1988. The Relationship between Plate Motions and Seismic Moment Tensors, and the Rates of Active Deformation in the Mediterranean and Middle East. Geophysical Journal 93, 45-73.

Jiménez-Muñoz, J.C., Sobrino, J.A.A. 2003. Generalized single-channel method for retrieving land surface temperature from remote sensing data. J. Geophys. Res. Atmos. 108, 4688.

Jimenez-Munoz, J. C., Sobrino, J. A., Skokovic, D., Mattar, C., Cristobal, J. 2014. Land surface temperature retrieval methods from Landsat-8 thermal infrared sensor data. IEEE Geosci Remote Sens Letter 11(10), 1840–1843.

Jolivet, L., Faccenna, C., Huet, B., Labrousse, L., Le Pourhiet, L., Lacombe, O., Lecomte, E., Burov, E., Denèle, Y., Brun, J.P., Philippon, M., Paul, A., Salaün, G., Karabulut, H., Piromallo, C., Monié, P., Gueydan, F., Okay, A.I., Oberhänsli, R., Pourteau, A., Augier, R., Gadenne, L., Driussi, O., 2013. Aegean tectonics: progressive strain localisation, slab tearing and trench retreat. Tectonophysics 597-598, 1–33. https://doi.org/10.1016/j.tecto.2012.06.011.

Kaya, O. 1978. Ege kıyı kuşağı (Dikili-Zeytindağı-Menemen-Yenifoça) Neojen stratigrafisi. Ege Üniversitesi Fen Fakültesi monografiler serisi, 17.

Kaçar, B., Özden, S., Ateş, Ö. 2017. Güre (Balıkesir) Jeotermal Alanının Jeolojisi, Hidrojeokimyası ve Aktif Tektonikle İlişkisi. Türkiye Jeoloji Bülteni 60, 243-258.

Karacık, Z., Yılmaz, Y. 1998. Geology of the ignimbrites and the associated volcanoplutonic complex of the Ezine area, Northwestern Anatolia. Journal of Volcanology and Geothermal Research 85 (1–4).

Kalinowski A., Oliver S. 2004. ASTER processing manual, Remote Sensing Applications, Geoscience Australia, internal report 39.

Kruse, F.A. 2012. Mapping surface mineralogy using imaging spectrometry. Geomorphology 137, 1, 41-56. https://doi.org/10.1016/j.geomorph.2010.09.032.

Kurtuluş, C., Doğan, B., Sertçelik, F., Canbay, M. M. 2009. Determination of the tectonic evolution of the Edremit Gulf based on seismic reflection studies. Marine Geophysical Research 30, 121–134.

Li, Z. L., Tang, B., Wu, H., Yan, G., W, Z., Trigo, I., Sobrino, J. 2013. Satellite-Derived Land Surface Temperature: Current Status and Perspectives. Remote Sensing of Environment 131, 14-37. 10.1016/j.rse.2012.12.008.

Littlefield, E., Calvin, W. 2014. Geothermal exploration using imaging spectrometer data over Fish Lake Valley, Nevada. Remote Sensing of Environment 140. 509–518. 10.1016/j.rse.2013.09.007.

Mazor, E. 1991. Applied chemical and isotopic groundwater hydrology. Open University Press, First Published, 264, Buckinghom.

McClusky, S., Balassanian, S., Barka, A. A., Demir, C., Ergintav, S., Georgiev, I., Gürkan, O., Hamburger, M., Hurst, K., Kahle, H., Kastens, K., Kekelidze, G., King, R., Kotzev, V., Lenk, O., Mahmoud, S., Mishin, A., Nadariya, M., Ouzounis, A., Paradissis, D., Peter, Y., Prilepin, M., Reilinger, R., Sanli, I., Seeger, H., Tealeb, A., Toksoz, M., Veis, G. 2000. Global positioning system constraints on plate kinematics and dynamics in the eastern Mediterranean and Caucasus. Journal of Geophysical Research 105(B3), 5695–5720.

McKenzie, D.P. 1972. Active tectonics of the Mediterranean region. Geophysical Journal of the Royal Astronomical Society 30, 109-158.

Mia, M. B., Nishijima, J., Fujimitsu, Y. 2014. Exploration and monitoring geothermal activity using Landsat ETM+images. A case study at Aso volcanic area in Japan. Journal of Volcanology and Geothermal Research 275. 10.1016/j.jvolgeores.2014.02.008.

Mia, M. B., Fujimitsu, Y., Nishijima, J. 2018. Monitoring of Thermal Activity at the Hatchobaru–Otake Geothermal Area in Japan Using Multi-Source Satellite Images-With Comparisons of Methods, and Solar and Seasonal Effects. Remote Sensing 10, 1430.

NASA. 2019. https://search.earthdata.nasa.gov/.

Norini, G., Groppelli, G., Sulpizio, R., Carrasco-Núñez, G., Davila-Harris, P., Pellicioli, C., Zucca, F., De Franco, R. 2015. Structural analysis and thermal remote sensing of the Los Humeros Volcanic Complex: Implications for volcano structure and geothermal exploration. Journal of Volcanology and Geothermal Research 301, 221-237. 10.1016/j.jvolgeores.2015.05.014.

Nukman, M., Moeck, I. 2013. Structural controls on a geothermal system in the Tarutung Basin, north central Sumatra. Journal of Asian Earth Sciences 74, 86-96. 10.1016/j.jseaes.2013.06.012.

Okay, A.I., Tüysüz, O. 1999. Tethyan sutures of northern Turkey. In: Durand, B., Jolivet, L., Horvath, F. and Seranne, M. (eds), Mediterranean Basins: Tertiary Extension within the Alpine Orogen. Geological Society, London, Special Publications 156, 475–515.

Okay, A. İ., Satır, M. 2000. Upper Cretaceous eclogite–facies metamorphic rocks from the Biga Peninsula, northwest Turkey. Turkish Journal of Earth Sciences 9, 47–56.

Okay, A. İ., Göncüoğlu, M. C. 2004. Karakaya complex: A review of data and concepts. Turkish Journal of Earth Sciences 13, 77–95.

Okay, A.İ., Siyako, M., Bürkan, K.A. 1990. Biga yarımadasının jeolojisi ve tektonik evrimi. Türkiye Petrol Jeologları Derneği Bülteni 2/1, 83-121.

Okay, A.İ., Siyako, M., Bürkan, K.A. 1991. Geology and tectonic evolution of the Biga Peninsula. Dewey, J.F. (ed). Special Issuse on tectonics. Bulletin of the Technical University of Istanbul 44, 191-255.

Okay, A. İ., Bozkurt, E., Satır, M., Yiğitbaş, E., Crowley, Q. G., Shang, C. K. 2008. Defining the southern margin of Avalonia in the Pontides: Geochronological data from the late Proterozoic and Ordovician granitoids from NW Turkey. Tectonophysics 461, 252–264.

Okay, A.İ., Satır, M., Maluski, H., Siyako, M., Monie, P., Metzger, R., Akyüz, S. 1996. Paleo and Neo-Tethyan events in northwest Turkey: Geological and geocronogical constraints. Yin, A., Harrisson, M. (Eds). Tectonics of Asia: Cambridge Üniv. Pres 420-441.

Ölmez, E., Gökalp, Y., Ertürk, İ., Ekici, S., Yıldız, Ş., Demirel, V., Sözen, İ. 2001. Balıkesir Edremit Derman Jeotermal Alanı ED1, ED2, ED3 Sondajları Kuyu Bitirme Raporu. Maden Tetkik ve Arama Genel Müdürlüğü Rapor No: 10512, Ankara (unpublished).

Özkaymak, Ç., Sözbilir, H., Uzel, B. 2013. Neogene-Quaternary evolution of the Manisa Basin: Evidence for variation in the stress pattern of the İzmir-Balıkesir Transfer Zone, western Anatolia. Journal of Geodynamics 65, 117–135.

Parastatidis, D., Mitraka, Z., Chrysoulakis, N., Abrams, M. 2017. Online global land surface temperature estimation from landsat. Remote Sensing 9(12), 1–16, doi:10.3390/rs9121208.

Pieri, D., Abrams, M. 2004. ASTER watches theworld's volcanoes: a newparadigm for volcanological observations from orbit. J. Volcanol. Geotherm. Research 135 (1-2), 13–28.

Pieri, D., Abrams, M. 2005. ASTER Observations of Thermal Anomalies Preceding the April 2003 Eruption of Chikurachki Volcano, Kurile Islands, Russia. Remote Sensing of Environment 99, 1-2, 2005. 84-94.

Piper, A. M. 1944. A Graphic Procedure in Geochemical Interpretation of Water Analyses, American Geophysical Union Transactions 25, 914-923.

Qin, Q., Zhang, N., Nan, P., Chai, L. 2011. Geothermal area detection using Landsat ETM+ thermal infrared data and its mechanistic analysis—A case study in Tengchong, China. Int. J. Appl. Earth Observation and Geoinformation 13(4), 552-559. doi:http://dx.doi.org/10.1016/j.jag.2011.

Ramírez-González, L. M., Aufaristama, M., Jónsdóttir, I., Hoskuldsson, A., Thordarson, T., Proietti, N., Kraft, G., Mcquilkin, J. 2019. Remote sensing of surface Hydrothermal Alteration, identification of Minerals and Thermal anomalies at Sveifluháls-Krýsuvík high-temperature Geothermal field, SW Iceland. 7th ITB International Geothermal Workshop (IIGW2018). IOP Conf. Series: Earth and Environmental Science 254, 012005. doi:10.1088/1755-1315/254/1/012005.

Reinisch, E., Cardiff, M., Kreemer, C., Akerley, J., Feigl, K. 2020. Time-series Analysis of Volume Change at Brady Hot Springs, Nevada, USA using Geodetic Data from 2003 – 2018. Journal of Geophysical Research: Solid Earth 125.

Rowan, L.C., Mars J.C. 2003. Lithologic mapping in the Mountain Pass, California area using Advanced Spaceborne Thermal Emission and Reflection Radiometer (ASTER) data. Remote Sensing of Environment 84, 350–366.

Rowan, L.C., Hook, S.J., Abrams, M.J., Mars, J.C. 2003. Mapping hydrothermally altered rocks at Cuprite, Nevada, using the Advanced Spacebourne Thermal Emission and Reflection Radiometer (ASTER), a new satellite-imaging system. Economic Geology 98, 1019–1027.

Sarp, S. Burçak, M., Yıldırım, T., Yıldırım, N. 1998. Biga Yarımadasının jeolojisi ve jeotermal enerji olanakları ile Balıkesir-Havran-Derman kaplıca sahasının detay jeotermal etüdü ve gradyan sondajları. Maden Tetkik ve Arama Genel Müdürlüğü Rapor No: 10537. Ankara (unpublished).

Sheng, J., Wilson, J., Lee, S. J. 2009. Comparison of land surface temperature (LST) modeled with a spatially-distributed solar radiation model (SRAD) and remote sensing data. Environmental Modelling & Software. 24. 436-443. 10.1016/j.envsoft.2008.09.003.

Siyako, M., Bürkan, K. A., Okay, A. I. 1989. Tertiary geology and hydrocarbon potential of the Biga and Gelibolu peninsulas (in Turkish). Türkiye Petrol Jeologları Derneği Bülteni 1, 183–200.

Sobrino, J., Jimenez-Munoz, J.C., Sòria B.G., Romaguera, M., Guanter, L., Moreno, J., Plaza, A., Martinez, P. 2008. Land surface emissivity retrieval from different VNIR and TIR sensors. Geoscience and Remote Sensing, IEEE Transactions on, 46, 316-327. 10.1109/TGRS.2007.904834.

Sobrino, J. A., Jiménez-Muñoz, J. C., Paolini, L. 2004. Land surface temperature retrieval from LANDSAT TM5. Remote Sensing Environment 90, 4, 434–440.

Song, B., Park, K. 2014. Validation of ASTER Surface Temperature Data with in Situ Measurements to Evaluate Heat Islands in Complex Urban Areas. Advances in Meteorology 1-12. 10.1155/2014/620410.

Srivastava, P.K., Majumdar, T.J., Bhattacharya, A.K. 2009, Surface Temperature Estimation in Singhbhum Shear Zone of India using Landsat-7 ETM+ Thermal Infrared Data. Advances in Space Research 43, 10, 1563-1574.

Straub, C., Kahle, H.-G., Schindler, C. 1997. GPS and geologic estimates of the tectonic activity in the Marmara region, NW Anatolia. J. Geophys. Res., 102, 27 587-27601.

Şengör, A.M.C., Yılmaz, Y. 1981. Tethyan evolution of Turkey, a plate tectonic approach. Tectonophysics 75, 181-241.

USGS. 2019. https://earthexplorer.usgs.gov/.

USGS. 2007. Spectral Library. https://www.usgs.gov/labs/spectroscopy-lab/science/spectral-library.

TJVT Database. 1:25.000 ölçekli Türkiye Jeoloji Veri Tabanı (TJVT) verileri. Maden Tetkik ve Arama Genel Müdürlüğü, Ankara, Türkiye.

Uzel, B., Sözbilir, H., Özkaymak, Ç., Kaymakçı, N., Langereis, C.G. 2013. Structural evidence for strike-slip deformation in the İzmir-Balıkesir transfer zone and consequences for late Cenozoic evolution of western Anatolia (Turkey). Journal of Geodynamics 65, 94-116.

Valor, E., Caselles, V. 1996. Mapping land surface emissivity from NDVI: Application to European, African, and South American areas. Remote Sensing Environment 57, 167–184.

Van de Griend, A., Owe, M. 1993. On the relationship between thermal emissivity and the normalized difference vegetation index for natural surfaces. Int. J. Remote Sens. 14, 1119–1131.

Van der Meer, F., Hecker, C., van Ruitenbeek, F., van der Werff, H., de Wijkerslooth, C., Wechsler, C. 2014. Geologic remote sensing for geothermal exploration: A review. Int. J. Appl. Earth Observation Geoinformation 33, 255-269.

Vaughan, R., Calvin, W., Taranik, J. 2003. SEBASS hyperspectral thermal infrared data: Surface emissivity measurement and mineral mapping. Remote Sensing of Environment 85, 48-63. 10.1016/S0034-4257(02)00186-4.

Vaughan, R., Lowenstern, J., Keszthelyi, L., Jaworowski, C., Heasler, H. 2012*a*. Mapping temperature and radiant geothermal heat flux anomalies in the yellowstone geothermal system using ASTER thermal infrared data. Transactions - Geothermal Resources Council 36, 1403-1409.

Vaughan, R.G., Keszthelyi, L.P., Lowenstern, J.B., Jaworowski, C., Heasler, H. 2012*b*. Use of ASTER and MODIS thermal infrared data to quantify heat flow and hydrothermal change at Yellowstone National Park. J. Volcanol. Geotherm. Research 233–234, 72–89.

Waswa, A. K. 2017. Mapping of Hydrothermal Minerals Related to Geothermal Activities Using Remote Sensing and GIS: Case Study of Paka Volcano in Kenyan Rift Valley. International Journal of Geosciences 8(05), 711-725.

Wang, Q., Mwirigi, M.M., Kinoshita, I. 2014. A GIS-Based Approach in Support of Spatial Planning for Renewable Energy: A Case Study of Fukushima, Japan. Sustainability 6, 2087-2117. 10.3390/su6042087.

Wessels, R.L., Vaughan, R.G., Patrick, M.R., Coombs, M.L. 2013. High-resolution satellite and airborne thermal infrared imaging of precursory unrest and 2009 eruption at Redoubt Volcano, Alaska. Journal of Volcanol. Geotherm. Research 259, 248–269.

Yalçın, T. 2007. Geochemical characterization of the Biga Peninsula thermal waters (NW Turkey). Aquatic Geochemistry 13, 75-93.

Yılmaz, Y., Karacık, Z. 2001. Geology of the northern side of the Gulf of Edremit and its tectonic significance for the development of the Aegean grabens. Geodinamica Acta 14, 31–43.

Yu, X., Xulin, G., Zhaocong, W. 2014. Land Surface Temperature Retrieval from Landsat 8 TIRS—Comparison between Radiative Transfer Equation-Based Method, Split Window Algorithm and Single Channel Method. Remote Sensing 6, 10: 9829-9852. https://doi.org/10.3390/rs6109829.

Zannina, J., Loriab, A. F. R., Llabjania, Q., Laloui, L. 2020. Extension of Winkler's solution to non-isothermal conditions for capturing the behaviour of plane geostructures subjected to thermal and mechanical actions. Computers and Geotechnics 128, 1-20.